May 22, 2018 | vol. 115 | no. 21 | pp. 5301–5618

PNAS

Proceedings of the National Academy of Sciences of the United States of America www.pnas.org

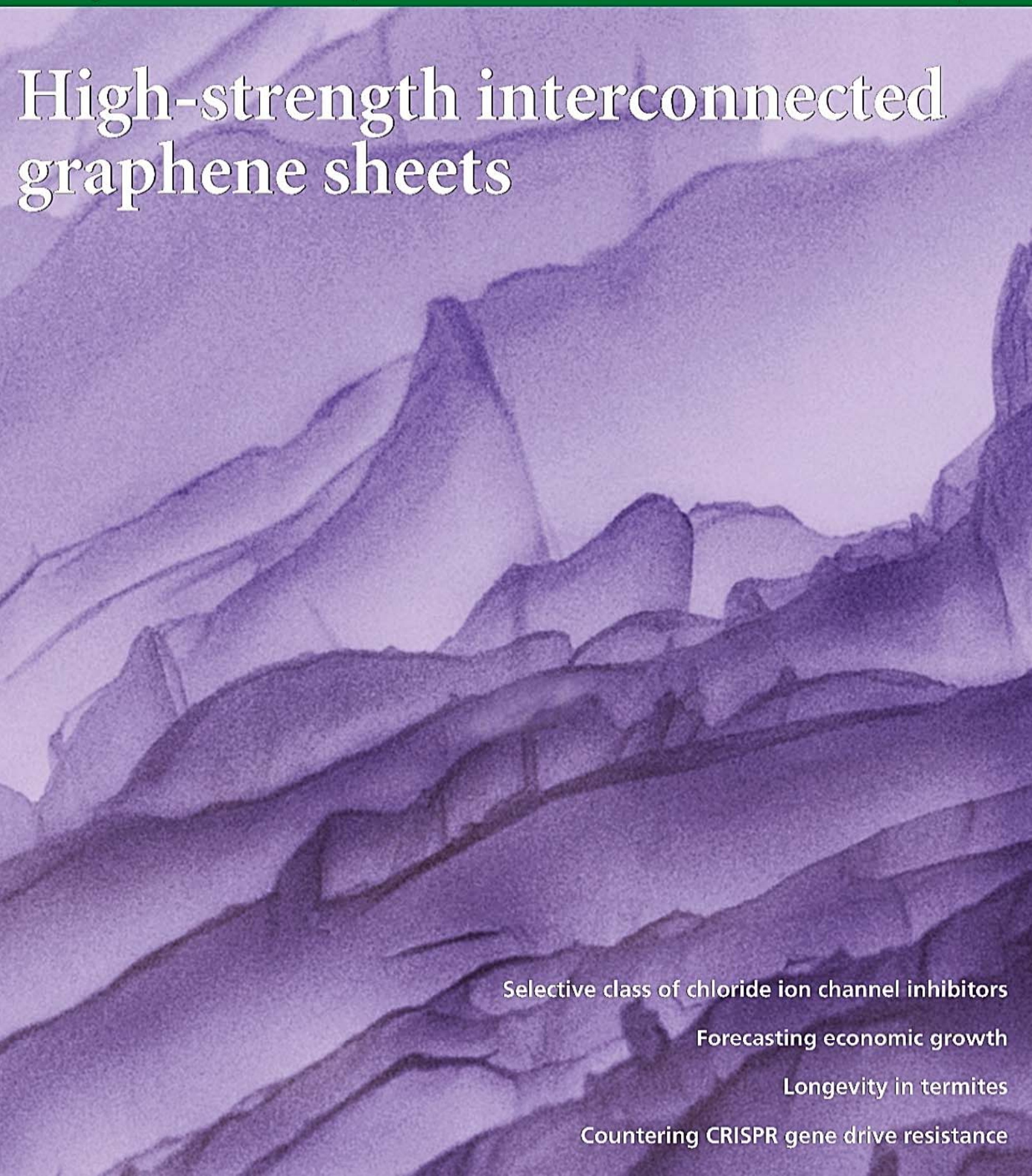

High-strength interconnected graphene sheets

Selective class of chloride ion channel inhibitors

Forecasting economic growth

Longevity in termites

Countering CRISPR gene drive resistance

Sequentially bridged graphene sheets with high strength, toughness, and electrical conductivity

Sijie Wan[a,b,1], Yuchen Li[a,b,1], Jiuke Mu[c,1], Ali E. Aliev[c], Shaoli Fang[c], Nicholas A. Kotov[b,d,e], Lei Jiang[a,b], Qunfeng Cheng[a,b,2], and Ray H. Baughman[c,2]

[a]Key Laboratory of Bio-inspired Smart Interfacial Science and Technology of Ministry of Education, School of Chemistry, Beihang University, 100191 Beijing, People's Republic of China; [b]Beijing Advanced Innovation Center for Biomedical Engineering, Beihang University, 100191 Beijing, People's Republic of China; [c]Alan G. MacDiarmid NanoTech Institute, University of Texas at Dallas, Richardson, TX 75080; [d]Department of Chemical Engineering, University of Michigan, Ann Arbor, MI 48109; and [e]Biointerface Institute, University of Michigan, Ann Arbor, MI 48109

Edited by Frans Spaepen, Harvard University, Cambridge, MA, and accepted by Editorial Board Member Tobin J. Marks March 28, 2018 (received for review November 3, 2017)

We here show that infiltrated bridging agents can convert inexpensively fabricated graphene platelet sheets into high-performance materials, thereby avoiding the need for a polymer matrix. Two types of bridging agents were investigated for interconnecting graphene sheets, which attach to sheets by either π–π bonding or covalent bonding. When applied alone, the π–π bonding agent is most effective. However, successive application of the optimized ratio of π–π bonding and covalent bonding agents provides graphene sheets with the highest strength, toughness, fatigue resistance, electrical conductivity, electromagnetic interference shielding efficiency, and resistance to ultrasonic dissolution. Raman spectroscopy measurements of stress transfer to graphene platelets allow us to decipher the mechanisms of property improvement. In addition, the degree of orientation of graphene platelets increases with increasing effectiveness of the bonding agents, and the interlayer spacing increases. Compared with other materials that are strong in all directions within a sheet, the realized tensile strength (945 MPa) of the resin-free graphene platelet sheets was higher than for carbon nanotube or graphene platelet composites, and comparable to that of commercially available carbon fiber composites. The toughness of these composites, containing the combination of π–π bonding and covalent bonding, was much higher than for these other materials having high strengths for all in-plane directions, thereby opening the path to materials design of layered nanocomposites using multiple types of quantitatively engineered chemical bonds between nanoscale building blocks.

graphene nanocomposites | cross-linked graphene | graphene oxide | covalent bonding agents | π–π bonding agents

Carbon fiber reinforced polymer composites are becoming ubiquitous in automotive, aviation, electronic, energy, and biomedical technologies. However, carbon fiber composites have many shortcomings that make their broader utilization challenging from both technical and economic standpoints. First, the mechanical properties of carbon fiber composites are anisotropic even when carbon fiber sheets are plied. Secondly, delamination of carbon fiber from the polymer matrix, especially in the seams with other materials, causes fractures that lead to failures. Thirdly, the electrical conductivity of carbon fiber composites is lower than desired for some applications.

Carbon-based nanomaterials, such as individual carbon nanotubes (CNTs) (1) and single graphene sheet (2), show extremely high mechanical and electrical properties due to their sp^2 bonding and nearly defect-free structure (3, 4). In the past decade, starting from the early examples (5, 6), various graphene-based composites (7–9), including thin sheets comprising graphene platelets (10–13), have been fabricated. However, improvements in mechanical and electrical properties are needed before inexpensive graphene-based composites can be used for high-performance applications. Instead of making a polymer composite in which graphene platelets are uniformly layered in a host polymer, we are designing a structure in which covalent and π–π interplatelet bonding provides bridges between adjacent graphene layers, and no host polymer resin is needed.

Herein, we demonstrate the fabrication of high-performance graphene-based sheets and the general method for their molecular engineering using versatile bridging chemistries. Using graphene oxide (GO) or reduced graphene oxide (rGO) platelets as the precursor, either the GO or rGO was sequentially exposed to agents that could bridge through π–π interactions or covalent bonding. These two bridging elements were added independently, which is convenient for optimizing performance by controlling the relative ratio of π–π interactions and covalent bonding. As a result, mechanical load is effectively transferred between rGO platelets in sequentially bridged graphene (SBG) composites, providing high strength, toughness, and electrical conductivity. The macroscale effect of nanoscale bridging is observed by the simultaneous improvements of various mechanical properties, as well as electrical conductivity, stability in harsh environments, and microwave shielding capabilities. Raman measurements demonstrate on a molecular scale the stress transfer that results in properties improvements.

Results and Discussion

Fig. 1*A* illustrates the process used to make SBG sheets. First, GO (*SI Appendix*, Fig. S1) dispersed in water was vacuum filtered to

Significance

There is a continuing search for manufacturable sheets having high strength and toughness in all sheet directions for diverse applications, from airplanes to windmills. Cross-plied carbon fibers in a polymer resin requiring high-temperature cure presently provide the common solution. We demonstrate cross-linked graphene sheets that are manufacturable from graphene platelets, which are resin-free, processable at low temperature, contain less than 10 wt % additives, and provide high strength and record toughness in all in-plane directions. This advance results from successive use of π–π and covalent cross-linking agents. Simultaneous enhancement of strength, durability, and electrical conductivity are demonstrated. Spectroscopic measurements, including Raman studies of interplatelet stress transfer, elucidate the chemical nature and physical consequences of these dual cross-linking agents.

Author contributions: Q.C. designed research; S.W., Y.L., J.M., A.E.A., S.F., and R.H.B. performed research; J.M., S.F., N.A.K., L.J., Q.C., and R.H.B. analyzed data; and S.W., S.F., Q.C., and R.H.B. wrote the paper.

The authors declare no conflict of interest.

This article is a PNAS Direct Submission. F.S. is a guest editor invited by the Editorial Board.

[1]S.W., Y.L., and J.M. contributed equally to this work.

[2]To whom correspondence may be addressed. Email: cheng@buaa.edu.cn or Ray.Baughman@utdallas.edu.

This article contains supporting information online at www.pnas.org/lookup/suppl/doi:10.1073/pnas.1719111115/-/DCSupplemental.

Published online May 7, 2018.

form a freestanding GO sheet. This sheet was immersed in a solution of 10,12-pentacosadiyn-1-ol [PCO, $CH_3(CH_2)_{11}C{\equiv}C{-}C{\equiv}C(CH_2)_8CH_2OH$] and then, after drying, exposed to UV light to provide a GO-PCO sheet in which the diacetylene groups of PCO have reacted by 1,4-addition polymerization (14, 15). Afterward, hydroiodic acid (HI) was used to reduce the GO-PCO sheets into graphene-PCO (G-PCO) sheets. Finally, the G-PCO sheet was immersed successively into 1-pyrenebutyric acid *N*-hydroxysuccinimide ester (PSE) and 1-aminopyrene (AP) solutions, thereby providing an SBG sheet in which the PSE and AP have bonded through π–π interactions with neighboring graphene platelets and reacted to provide PSE-AP covalent bonds (16). The ratio of π–π interactions through PSE-AP derived bonding and covalent bonding resulting from PCO can be optimized by adjusting the immersion times in the respective solutions. To compare properties, sheets were also obtained by eliminating treatment with PCO, thereby providing sheets that are π-bridged graphene (πBG).

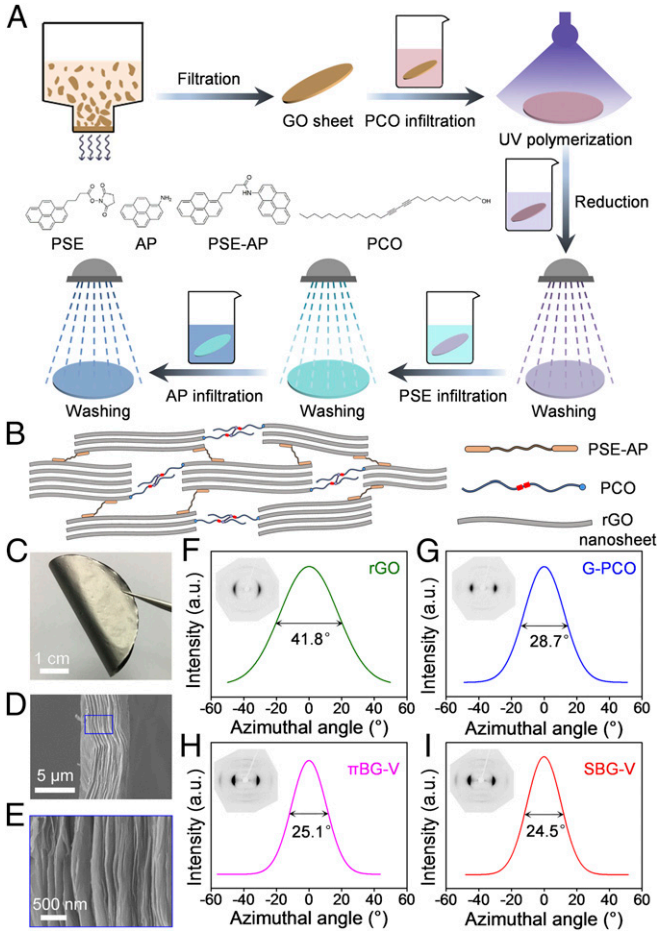

Fig. 1. Fabrication and structural characterization of SBG sheets. (*A*) GO platelets were assembled into a GO sheet by filtration, and then PCO was infiltrated into the GO sheet and polymerized using UV radiation. Next, the GO-PCO was reduced using HI. Afterward, PSE and AP were successively infiltrated into the sheet, which resulted in their reaction to form PSEAP molecules, which are able to π-bond on rGO layers. (*B*) Schematic structural model showing possibly resulting edge connection between rGO layers in different platelets within an SBG sheet. *SI Appendix*, Fig. S3 illustrates 1,4-addition reaction of diacetylene layers on the top of a platelet, which can provide covalent bonding between neighboring platelet surfaces. (*C*) Photograph of an SBG sheet, showing its flexibility. (*D*) Low-resolution SEM image of the edge of a fractured SBG sheet. (*E*) High-resolution SEM image of the area outlined in *D*. WAXS patterns for an incident beam parallel to the sheet plane and corresponding azimuthal scan profiles for 002 peak for (*F*) rGO, (*G*) G-PCO, (*H*) πBG-V, and (*I*) SBG-V sheets.

The combination of these bridging agents, using optimized relative concentrations, provides the difficult-to-attain combination of strength and toughness for a structure having isotropic in-plane mechanical properties. Previous investigations led to our choice of the individual bridging agents. Over two decades ago, Katz (17) demonstrated the use of the strong π-bonding of PSE to pyrolytic graphite for protein immobilization, and deployed an extrusion reaction to enable direct coupling between the carbonyl group of PSE and a NH group of a protein, like for the present reaction with AP to form PSE-AP (Fig. 1*A*). AP is well known to strongly bond with graphitic surfaces (18). Using AP with another reactive π-bonding agent, thin sheets having a tensile strength of 539 MPa were obtained (19). Scanning tunneling microscopy has shown that the diacetylene monomer PCO polymerizes by 1,4-addition reaction on graphite sheets (20) and polymerized PCO has been used to increase the realized modest tensile strengths (220 MPa) for stretched CNT sheets (15). Polymerized PCO has also been used to cross-couple rGO nanosheets to provide a maximum tensile strength of 157 MPa (14).

Schematic illustrations are provided for 1,4-addition polymerization of PCO to yield covalent connectivity between platelet edges of rGO (Fig. 1*B* and *SI Appendix*, Fig. S2) and between the basal planes of neighboring graphene platelets (*SI Appendix*, Fig. S3). Spectroscopic evidence for these bridging processes and resulting property improvements will be described later. After PCO infiltration, the hydroxyl group on one end of the PCO monomers can covalently graft to GO nanosheets by reaction with carboxyl groups on the GO nanosheets. Then, PCO molecules grafted on nearby GO platelets are covalently coupled by 1,4-addition polymerization of diacetylene groups using UV irradiation (Fig. 1*B* and *SI Appendix*, Figs. S2 and S3). Subsequent HI reduction removes most of the unreacted oxygen-containing groups on the surface of GO nanosheets. After successive PSE and AP infiltration, the PSE and AP react to form PSE-AP (shown in Fig. 1*B*), which provides at opposite PSE-AP ends the aromatic functionalities needed for the π–π interactions that enable bridging between nearby rGO nanosheets.

Since X-ray diffraction measurements (*SI Appendix*, Table S1) indicate that the interplanar spacing within π–π bonded, covalently bonded, and sequentially bonded platelets are atomically thin (between 3.70 and 3.81 Å, and close to the 3.66 Å for dry rGO), it is clear that the PCO and PSE-AP bonding agents provide structural reinforcement by coating the surfaces of rGO platelets, rather than intercalating the platelets. These binding agents can thereby potentially connect platelet edges (both interplatelet and intraplatelet) and connect the exterior basal planes of stacked platelets. Since the ratio of the surface area available on exterior platelet basal planes to that on platelet edges is very large (on the order of 4,000, based on the measurement results in *SI Appendix*, Fig. S1 for exfoliated graphene oxide), we suspect that edge-based coupling (like exclusively illustrated in Fig. 1*B* for PCO-based covalent coupling) is unimportant. Moreover, the topochemical 1,4-addition polymerization of a diacetylene monomer critically depends on the assembly of PCO into an ordered array, and such assembly (illustrated in *SI Appendix*, Fig. S3) is likely facilitated by the roughly planar geometry of the exterior basal planes of GO platelets.

Five kinds of SBG sheets were prepared: SBG-I to SBG-V. The content of PSE-AP and PCO molecules (*SI Appendix*, Table S2) in these flexible silver-gray sheets (Fig. 1*C*) was derived from thermogravimetric analysis curves (*SI Appendix*, Fig. S4). Fig. 1 *D* and *E* shows low- and high-resolution scanning electron microscope (SEM) images of SBG-V (containing 3.98 wt % PCO and 5.43 wt % PSE-AP), which are similar to the images for the other investigated SBG samples (*SI Appendix*, Fig. S5). The energy-dispersive X-ray spectroscopy mapping of nitrogen

element, which was performed on the cross-section of SBG-V sheets (*SI Appendix*, Fig. S6), demonstrates the infiltration of PSE-AP within the rGO sheet. As expected from the layered structure shown in these SEM images, a strong diffraction peak corresponding to the interlayer separation within platelets is observed in X-ray diffraction curves (*SI Appendix*, Fig. S7). The degree of platelet orientation is indicated by the wide-angle X-ray scattering (WAXS) patterns (Fig. 1 *F*–*I*), which were obtained by using an incident X-ray beam that is parallel to the sheet plane. These measurements provide the full width at half maximum measured in azimuthal scans for the 002 peak (41.8°, 28.7°, 25.1°, and 24.5° for rGO, G-PCO, πBG-V, and SBG-V, respectively).

Hence, reduced graphene oxide platelet orientation is improved by interplate bridging compared with other biomimetic composites studied before (21), and a high degree of orientation was obtained for the SBG-V, as tabulated in *SI Appendix*, Table S3. Interestingly, the SBG-V (3.81 Å) and πBG-V (3.80 Å) sheets provide longer interlayer diffraction spacings (*SI Appendix*, Table S1) than found for rGO (3.66 Å) and G-PCO (3.72 Å). This longer spacing might result from stresses produced by bonding agents that interconnect neighboring graphene platelets. Most importantly, the interplanar spacings for all of these π–π bonded, covalently bonded, and sequentially bonded rGO platelets are so small (*SI Appendix*, Table S1) that it is clear that these bridging agents do not appreciably intercalate between platelet layers. Instead, these bonding agents attach to the external surfaces of platelets of stacked graphene, thereby enabling bridging between platelets.

Compared with rGO sheets, the bridged graphene sheets show increased resistance to destruction under ultrasonication (100 W, 40 kHz) in various solutions, such as *N*-methyl-2-pyrrolidone (NMP), dimethylformamide (DMF), water, sulfuric acid (H_2SO_4), and sodium hydroxide (NaOH) aqueous solutions, as shown in Fig. 2. Specifically, for all solutions the stability of the sheet structure with respect to damage produced by ultrasonication was as follows: SBG-V > πBG-V > G-PCO sheets. NMP and DMF, whose surface energy is well matched to that of graphene, more effectively provides ultrasonication-produced sheet disintegration than do the other liquids (22, 23). Photographs showing the time dependence or ultrasonic sheet disintegration in various liquids are provided in *SI Appendix*, Figs. S8–S12, and the results are summarized in *SI Appendix*, Fig. S13.

As a result of sequential bridging, SBG-V sheets provide a tensile strength (944.5 ± 46.6 MPa) and toughness (20.6 ± 1.0 MJ·m^{-3}) that are higher than for πBG-V sheets (688.5 ± 17.0 MPa and 16.6 ± 1.2 MJ·m^{-3}), G-PCO sheets (348.5 ± 12.0 MPa and 8.5 ± 1.3 MJ·m^{-3}), or rGO sheets (209.7 ± 8.0 MPa and 2.6 ± 0.1 MJ·m^{-3}), as tabulated in *SI Appendix*, Table S4. Also, the low-strain Young's modulus of SBG-IV (18.5 GPa) and SBG-V (15.6 GPa) are substantially higher than for rGO (8.0 GPa), πBG-V (11.1 GPa), and G-PCO (5.3 GPa) as shown in Fig. 3*A* and *SI Appendix*, Fig. S14 and Table S5. Fig. 2 shows that sheet toughness monotonically increases with increasing sheet strength and that the structure retention time with respect to ultrasonic disintegration increases monotonically for all liquids with increasing sheet strength.

Gravimetric sheet strengths can be calculated by normalizing the measured sheet strengths to the measured sheet densities, which vary over only a 3% range (*SI Appendix*, Table S4) for rGO (2.01 g/cm^3), G-PCO (2.03 g/cm^3), πBG-V (2.04 g/cm^3), and SBG-V (2.07 g/cm^3). Measurement reliability is confirmed by comparing these gravimetric strengths and those derived by normalizing the fracture force to the sample weight per sample length, which are (respectively, in N·m·g^{-1}), 104.3 ± 4.0 and 108.6 ± 5.1 for rGO, 171.7 ± 5.9 and 176.4 ± 7.2 for G-PCO, 337.5 ± 8.3 and 341.8 ± 9.5 for πBG-V, and 456.3 ± 22.5 and 459.8 ± 19.4 for SBG-V. As a minor point, note that the SEM images of fracture surfaces show curling of platelet edges for the bridged graphene samples, but not for the samples of rGO (*SI Appendix*, Fig. S15). This curling might be a consequence of enhanced interplatelet bonding in the bridged composites.

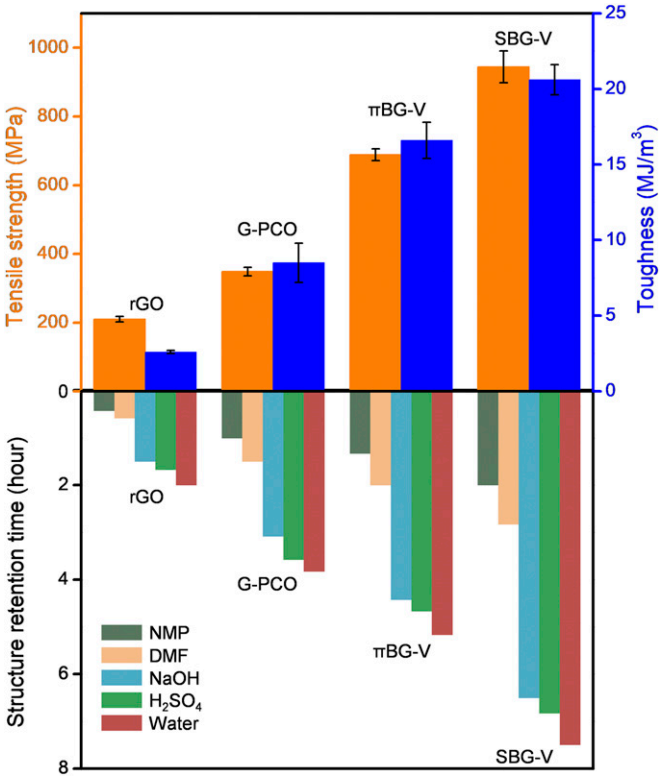

Fig. 2. (*Top*) Correspondence between tensile strength and toughness of the rGO, G-PCO, πBG-V, and SBG-V sheets is indicated. (*Bottom*) Results show for these sheet types the time required for the first appearance of sheet fragmentation during ultrasonication (100 W at 40 kHz) in NMP, (DMF), NaOH (with OH^- concentration of 8 mol·L^{-1}), H_2SO_4 (with H^+ concentration of 8 mol·L^{-1}), and water. Note for each of these solutions that this structure retention time increases monotonically with increase in sheet strength.

With a strength approaching 1 GPa, the SBG-V sheets are stronger than reported for graphene-platelet–based sheet composites (10–14, 24–37) (Fig. 3*B*). They also have a comparable or higher strength than commercially available carbon fiber composites that are plied to have high strengths in all sheet plane directions (www.hexcel.com/Resources/DataSheets/Prepreg) (such as T300-3K-PW/F655 BMI, T300-3K-8HS/F593 epoxy, and T700-12K-Twill/M47 epoxy) and a higher strength than reported for CNT sheet composites having in-plane tensile strength isotropy (6, 38–42). Most importantly, none of the above carbon composites have a toughness that rivals SBG-V. The detailed mechanical properties of these materials are tabulated in *SI Appendix*, Table S6. While the toughness for the SBG-V sheets is much lower than for fibers comprising a dispersion of rGO and single-walled CNTs in polyvinyl alcohol (43), these uniaxial fibers lack the isotropic sheet plane toughness of the dual-bridged SBG-V. In addition, even though the absolute strength for the SBG-V sheets is lower than for recently reported ultrastrong metal alloys (44, 45), they provide a higher gravimetric strength than for these metal alloys (46–48), as shown in Fig. 3*C*.

The Fourier transform infrared (FTIR) spectra (*SI Appendix*, Fig. S16*A*) of πBG-V and SBG-V contain features around 3,248.8 cm^{-1} and 1,666.3 cm^{-1}, respectively, for the N–H and C = O in amide groups of PSE-AP (*SI Appendix*, Fig. S16*B*), which indicates that PSE and AP have reacted to form amide linkages (16). In addition, the FTIR results for G-PCO and SBG-V (*SI Appendix*, Fig. S16*A*) show strong absorption peaks at

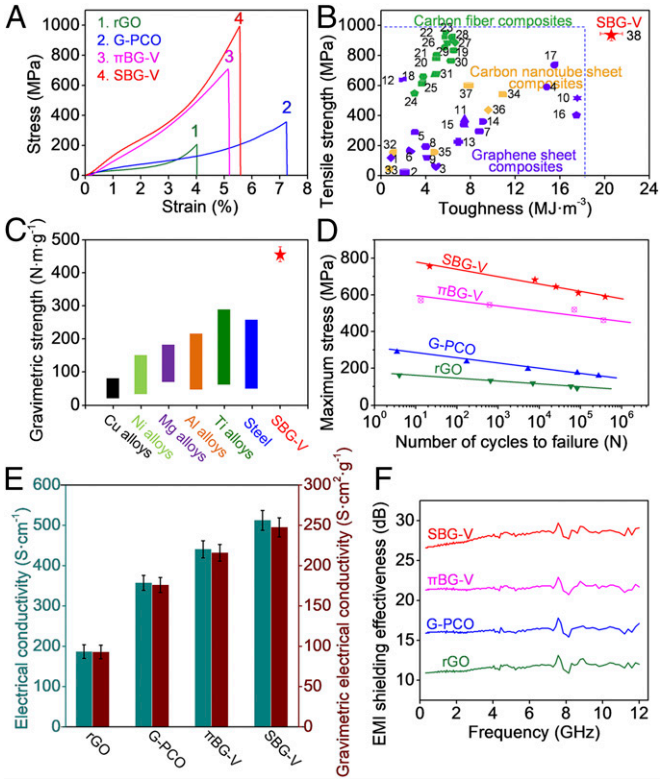

Fig. 3. Properties of SBG sheets. (*A*) Representative stress–strain curves for sheets of (1) rGO, (2) G-PCO, (3) πBG-V, and (4) SBG-V. (*B*) Comparison of the tensile strength and toughness of an SBG-V sheet (red star) with the tensile strength and toughness of other materials having high strengths in all sheet plane directions: carbon fiber composites (green symbols), CNT sheet composites (orange symbols), and graphene sheet composites (purple symbols). (*C*) Comparison of the gravimetric strength of SBG-V sheets with the gravimetric strength of metals, where the base and top of the data bars indicate the range of gravimetric strengths. (*D*) Dependence of the number of cycles to failure on the maximum stress level for rGO, G-PCO, πBGV, and SBG-V sheets. (*E*) Comparison of gravimetric electrical conductivity (red) and absolute electrical conductivity (green) for rGO, G-PCO, πBG-V, and SBG-V sheets. (*F*) EMI shielding effectiveness as a function of frequency for rGO, G-PCO, πBG-V, and SBG-V sheets having thicknesses between 3.3 and 3.8 μm.

1,770.4 cm^{-1} and 1,168.7 cm^{-1}, corresponding to the C = O and −C−O−C− in ester groups, respectively. These peaks likely result from the reaction of the −OH groups of PCO with oxygen-containing groups of the GO during the synthesis of SBG-V and G-PCO (14).

Raman spectra (*SI Appendix*, Fig. S17*A*) show that the C≡C vibration of GO-PCO sheets is down-shifted from 2,260 to 2,119 cm^{-1} after UV irradiation, demonstrating the 1,4-addition polymerization of PCO (49). The corresponding shift in the Raman frequency of the neat monomer upon UV irradiation (*SI Appendix*, Fig. S17*B*) is nearly identical (from 2,258 to 2,120 cm^{-1}). This downshifted C≡C vibration is also seen at 2,119 cm^{-1} for SBG-V and G-PCO (*SI Appendix*, Fig. S17*C*), indicating that the polydiacetylene chains remain after reduction of the GO-PCO. Note that the C = C stretch frequency, which is observed in UV-irradiated neat PCO (*SI Appendix*, Fig. S17*B*), is not observed for UV-irradiated GO-PCO sheets, which is likely a consequence of the overwhelmingly strong G band of graphene sheets in the C = C vibration region and the low PCO content. The UV-visible spectra (*SI Appendix*, Fig. S18) of UV-irradiated neat PCO and GO-PCO sheets show absorption peaks at 538 and 608 nm and at ∼540 and ∼612 nm, respectively, which further verifies the polymerization of PCO to form long conjugated polymer chains (50). For nonpolarized light propagating normal to the sheet plane, the ability to observe the Raman spectra due to low concentrations of polydiacetylene bridging agents, as well as the absorption due to long conjugation length polydiacetylene chains, confirms that interplatelet bridging results from the polymerization of long diacetylene arrays that assemble on the basal plane surfaces of rGO platelets.

The improved mechanical properties (*SI Appendix*, Table S5), as well as the improved resistance to mechanical damage during ultrasonication, suggest that PCO groups in the polydiacetylene chain have reacted with neighboring rGO platelets to provide covalent interplatelet bonding. Compared with rGO and G-PCO sheets, the Raman spectra of πBG-V and SBG-V sheets (*SI Appendix*, Fig. S17 *C–E*) show a slightly down-shifted G-band frequency (from 1,581 to 1,578 cm^{-1}) and a slightly up-shifted 2D band frequency (from 2,684 to 2,690 cm^{-1}). Interestingly, the *D*/*G* Raman intensity ratio (*SI Appendix*, Table S7) of rGO, G-PCO, πBG-V, and SBG-V sheets are similar (between 1.61 and 1.69), suggesting a negligible effect of the bridging agents on the conjugated structure of rGO sheets (16).

X-ray photoelectron spectroscopy (XPS) (*SI Appendix*, Fig. S19) shows that the C–C peak of sp^2 carbon is slightly up-shifted from 284.7 eV for sheets of GO, rGO, GO-PCO, and rGO-PCO to 285.1 eV for sheets of πBG-V and SBG-V. Most importantly, a C−N peak due to amide groups arises at 286.2 eV for πBG-V and SBG-V, which indicates reaction between PSE and AP. Additionally, the XPS data show that the O_{1s}/C_{1s} ratio decreases from 0.41 and 0.45 for GO and GO-PCO sheets to 0.16–0.19 for rGO, πBG-V, G-PCO, and SBG-V sheets (*SI Appendix*, Table S8), indicating the substantial reduction of oxygen-containing groups of GO sheets during reduction by HI (51–53).

Besides providing remarkable static mechanical properties, the sequential bridging of π-bonding and covalent bonding in SBG sheets also increases the fatigue resistance of SBG sheets. Fig. 3*D* shows the dependence of the cycle life on the maximum applied stress. These results show that SBG-V sheets have higher cycle life for all applied stresses than the rGO, G-PCO, and πBG-V sheets. While both the G-PCO and πBG-V sheets have higher fatigue resistance than rGO, the fatigue resistance for πBG-V is much higher than for G-PCO. This especially enhanced fatigue resistance of πBG-V might be due to the ability of π–π bonding to behave as

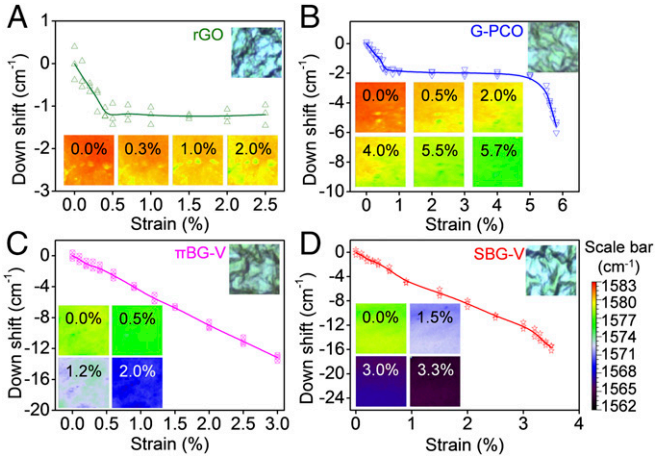

Fig. 4. Dependence of Raman frequency down-shifts on applied strain. (*A*) rGO, (*B*) G-PCO, (*C*) πBG-V, and (*D*) SBG-V sheets. Optical images of the sheets at zero strain are in the upper right-hand corners. The images in the below left-hand corners show the spatial distribution of Raman frequencies. All images are of a 400-μm^2 square area. The scale bar indicates the relationship between the color in the images and the Raman frequency.

sacrificial bonds that break and reform dynamically during fatigue testing. Such behavior is similar to that of some tough biological materials (54), which are able to dissipate much more energy than materials having predominantly strong covalent bonding. This observation is conducive with biomimetic engineering of these layered compounds enhanced by optimized bridging. Stress–strain curves during cycling and fracture morphologies after fatigue fracture are shown in *SI Appendix*, Fig. S20.

Consistent with the improved organization of the graphene-based nanocomposites (55), the bridging also increases the electrical conductivity and the electromagnetic interference (EMI) shielding efficiency of rGO sheets. More specifically, the successively bridged sheet sample SBG-V provides the highest electrical conductivity (512.3 ± 24.5 $S{\cdot}cm^{-1}$, Fig. 3*E* and *SI Appendix*, Table S4), the highest gravimetric electrical conductivity (247.5 ± 11.8 $S{\cdot}cm^2{\cdot}g^{-1}$), and the highest EMI shielding efficiency (Fig. 3*F*). Note that the electrical conductivity of SBG-V sheets is lower than for recently reported high-temperature-annealed graphene sheets (11) and graphene sheet composites composed of almost-intact graphene nanosheets (30). For comparison, the electrical conductivity and gravimetric electrical conductivity of rGO, G-PCO, and πBG-V are 186.8 ± 16.9 $S{\cdot}cm^{-1}$ and 92.9 ± 8.4 $S{\cdot}cm^2{\cdot}g^{-1}$, 357.2 ± 18.6 $S{\cdot}cm^{-1}$ and 176.0 ± 9.2 $S{\cdot}cm^2{\cdot}g^{-1}$, and 440.5 ± 21.3 $S{\cdot}cm^{-1}$ and 215.9 ± 10.4 $S{\cdot}cm^2{\cdot}g^{-1}$, respectively. Reflecting the high electrical conductivity of SBG-V, the EMI shielding effectiveness of SBG-V sheets (∼27 dB) in the frequency range between 0.3 and 12 GHz is higher than for similarly thick rGO (∼11 dB), G-PCO (∼16 dB), and πBG-V (∼21 dB) sheets. While the EMI shielding efficiency of SBG-V sheets is inferior to other state-of-the-art EMI shielding materials (56), it is still higher than for previously reported graphene sheets (57–59) having similar thicknesses, and is in the range of commercial interest.

Raman measurements of the strain dependence (60) of the graphene G-band frequency provide interesting information on the differences in stress transfer for rGO, G-PCO, πBG-V, and SBG-V sheets (61–64) (Fig. 4). Both rGO and G-PCO provide long plateaus in which Raman frequency is independent of the macroscopically applied strain. This plateau is between ∼0.4% and ∼2.5% strain for rGO sheets and between ∼0.6% and ∼5% strain for G-PCO sheets, where the upper strain limit corresponds to sheet fracture for rGO and is slightly below the strain of complete fracture for G-PCO (∼5.8%). These results show that while PCO substantially increases the strain to failure, it does not enable efficient stress transfer to the graphene sheets in the plateau region. In contrast, the πBG-V and SBG-V sheets do not have a plateau region in Raman frequency shift. This fact and the larger strain dependence of Raman shift for πBG-V and SBG-V sheets than for rGO or G-PCO sheets indicate more efficient stress transfer to the graphene sheets. Note that the failure stress and the Raman frequency shift up to failure strain are 209.7 MPa and ∼1.2 cm^{-1} for rGO, 348.5 MPa and ∼5.6 cm^{-1} for G-PCO, 688.5 MPa and ∼13.2 cm^{-1} for πBG-V, and 944.5 MPa and ∼15.7 cm^{-1} for SBG-V. Hence, both the observed Raman shifts and the measured tensile strength indicate improved stress transfer for πBG-V and SBG-V sheets compared with that for rGO and G-PCO sheets.

The Raman frequency shifts are reversible for all of the presently investigated graphene sheet compositions as long as the applied strain does not exceed ∼0.4% (*SI Appendix*, Fig. S21), which might correspond to elastic deformability due to straightening of rGO platelets. While there is no significant higher strain range where strain release reverses without hysteresis the strain-induced Raman frequency down-shift for rGO, this strain range exists for strains down to ∼5.4% for G-PCO stretched to 5.75%, for strains down to ∼1.5% for πBG-V stretched to 2.0%, and for strains down to ∼2.9% for SBG-V stretched to 3.4%. This elastic behavior with respect to the stretch applied to the graphene sheets (as measured by Raman frequency shifts) might result from elastic strain release due to covalent bonding, π–π bonding, and some combination of π–π and covalent bonding.

The sequential application of two bridging agents has enabled the scalable fabrication of resin-free composites having a combination of multiple properties including both mechanical and charge-transport characteristics. The realized tensile strength (945 MPa) exceeds that of previously reported CNT or graphene platelet composites that are strong in all sheet plane directions, and is comparable to that of commercially available carbon fiber sheet composites that are plied to increase strength in all in-plane directions. The toughness of our composites containing the combination of π–π bonding and covalent bonding was much higher than for these other materials having high strength in all sheet directions and they can be made at low processing temperatures. The combination of π–π bonding and covalent bonding bridging agents is more effective than the application of either agent. The strain dependence of Raman frequency indicate the effectiveness of π-bonded and covalently bonded agents in distributing local stress and can help address fundamental questions about structural relationship between nanosheet interfaces and the macroscale mechanics of biomimetic composites. SBG composites might provide the next generation of lightweight functional composites that are needed for addressing the problems facing several key industries.

Materials and Methods

The PCO was received from Tokyo Chemical Industry Co., Ltd., and PSE, AP, and HI (57 wt %) were purchased from Sigma-Aldrich. THF (≥99.0%), NMP (≥99.0%), DMF (≥99.5%), H_2SO_4, NaOH, and ethanol (≥99.7%) were obtained from Sinopharm Chemical Reagents Co., Ltd. These reagents were used as received without further purification. Deionized water (resistivity >18 MΩ·cm) was collected from a Mili-Q Biocel system. GO was prepared by modified Hummer's method (12) and dried for the following experiments. More details on the materials and methods can be found in *SI Appendix*.

ACKNOWLEDGMENTS. We thank Professor Juan José Vilatela at Madrid Institute for Advanced Studies of Materials for WAXS measurements, and thank Professor Jiaxing Huang at Northwestern University for helpful discussion. This work was supported by the Excellent Young Scientist Foundation of the National Natural Science Foundation of China (NSFC) (Grant 51522301), the NSFC (Grants 21273017 and 51103004), the Program for New Century Excellent Talents in University (Grant NCET-12-0034), the Fok Ying-Tong Education Foundation (Grant 141045), the 111 Project (Grant B14009), the Aeronautical Science Foundation of China (Grants 20145251035 and 2015ZF21009), State Key Laboratory of Organic-Inorganic Composites, Beijing University of Chemical Technology (Grant oic-201701007), the State Key Laboratory for Modification of Chemical Fibers and Polymer Materials, Donghua University (Grant LK1710), the Fundamental Research Funds for the Central Universities (Grants YWF-16-BJ-J-09 and YWF-17-BJ-J-33), and the Academic Excellence Foundation of Beihang University for PhD Students. Support in the United States was from Air Force Office of Scientific Research Grants FA9550-15-1-0089 and FA9550-12-1-0035 and NSF Award 1636306.

1. Iijima S (1991) Helical microtubules of graphitic carbon. *Nature* 354:56–58.
2. Novoselov KS, et al. (2004) Electric field effect in atomically thin carbon films. *Science* 306:666–669.
3. Du X, Skachko I, Barker A, Andrei EY (2008) Approaching ballistic transport in suspended graphene. *Nat Nanotechnol* 3:491–495.
4. Lee C, Wei X, Kysar JW, Hone J (2008) Measurement of the elastic properties and intrinsic strength of monolayer graphene. *Science* 321:385–388.
5. Kotov NA, Dékány I, Fendler JH (1996) Ultrathin graphite oxide–polyelectrolyte composites prepared by self-assembly: Transition between conductive and non-conductive states. *Adv Mater* 8:637–641.
6. Mamedov AA, et al. (2002) Molecular design of strong single-wall carbon nanotube/polyelectrolyte multilayer composites. *Nat Mater* 1:190–194.
7. Wan SJ, Cheng QF (2017) Fatigue-resistant bioinspired graphene-based nanocomposites. *Adv Funct Mater* 27:1703459.
8. Wan S, Peng J, Jiang L, Cheng Q (2016) Bioinspired graphene-based nanocomposites and their application in flexible energy devices. *Adv Mater* 28:7862–7898.
9. Zhang Y, et al. (2016) Graphene-based artificial nacre nanocomposites. *Chem Soc Rev* 45:2378–2395.
10. Xiao Y, et al. (2017) Sheet collapsing approach for rubber-like graphene papers. *ACS Nano* 11:8092–8102.

11. Peng L, et al. (2017) Ultrahigh thermal conductive yet superflexible graphene films. *Adv Mater* 29:1700589.
12. Zhang M, et al. (2015) Multifunctional pristine chemically modified graphene films as strong as stainless steel. *Adv Mater* 27:6708–6713.
13. Liu Z, et al. (2014) Wet-spun continuous graphene films. *Chem Mater* 26:6786–6795.
14. Cheng Q, Wu M, Li M, Jiang L, Tang Z (2013) Ultratough artificial nacre based on conjugated cross-linked graphene oxide. *Angew Chem Int Ed Engl* 52:3750–3755.
15. Chen IWP, Liang R, Zhao H, Wang B, Zhang C (2011) Highly conductive carbon nanotube buckypapers with improved doping stability via conjugational cross-linking. *Nanotechnology* 22:485708.
16. Chen IWP (2013) Noncovalently functionalized highly conducting carbon nanotube films with enhanced doping stability via an amide linkage. *Chem Commun (Camb)* 49: 2753–2755.
17. Katz E (1994) Application of bifunctional reagents for immobilization of proteins on a carbon electrode surface: Oriented immobilization of photosynthetic reaction centers. *J Electroanal Chem* 365:157–164.
18. Wang S, Wang X, Jiang SP (2008) PtRu nanoparticles supported on 1-aminopyrene-functionalized multiwalled carbon nanotubes and their electrocatalytic activity for methanol oxidation. *Langmuir* 24:10505–10512.
19. Ni H, et al. (2017) Robust bioinspired graphene film via π-π cross-linking. *ACS Appl Mater Interfaces* 9:24987–24992.
20. Takajo D, Inaba A, Sudoh K (2014) Two-dimensional solid-state topochemical reactions of 10,12-pentacosadiyn-1-ol adsorbed on graphite. *Langmuir* 30:2738–2744.
21. Wegst UGK, Bai H, Saiz E, Tomsia AP, Ritchie RO (2015) Bioinspired structural materials. *Nat Mater* 14:23–36.
22. Coleman JN (2013) Liquid exfoliation of defect-free graphene. *Acc Chem Res* 46: 14–22.
23. Hernandez Y, et al. (2008) High-yield production of graphene by liquid-phase exfoliation of graphite. *Nat Nanotechnol* 3:563–568.
24. Cui W, et al. (2014) A strong integrated strength and toughness artificial nacre based on dopamine cross-linked graphene oxide. *ACS Nano* 8:9511–9517.
25. Gong S, et al. (2015) Integrated ternary bioinspired nanocomposites via synergistic toughening of reduced graphene oxide and double-walled carbon nanotubes. *ACS Nano* 9:11568–11573.
26. Wan S, et al. (2015) Synergistic toughening of graphene oxide-molybdenum disulfide-thermoplastic polyurethane ternary artificial nacre. *ACS Nano* 9:708–714.
27. Wan S, et al. (2015) Use of synergistic interactions to fabricate strong, tough, and conductive artificial nacre based on graphene oxide and chitosan. *ACS Nano* 9: 9830–9836.
28. Wan S, et al. (2017) Fatigue resistant bioinspired composite from synergistic two-dimensional nanocomponents. *ACS Nano* 11:7074–7083.
29. Li YQ, Yu T, Yang TY, Zheng LX, Liao K (2012) Bio-inspired nacre-like composite films based on graphene with superior mechanical, electrical, and biocompatible properties. *Adv Mater* 24:3426–3431.
30. Wen Y, Wu M, Zhang M, Li C, Shi G (2017) Topological design of ultrastrong and highly conductive graphene films. *Adv Mater* 29:1702831.
31. Xiong R, et al. (2016) Ultrarobust transparent cellulose nanocrystal-graphene membranes with high electrical conductivity. *Adv Mater* 28:1501–1509.
32. Zhang M, Huang L, Chen J, Li C, Shi G (2014) Ultratough, ultrastrong, and highly conductive graphene films with arbitrary sizes. *Adv Mater* 26:7588–7592.
33. Wan SJ, Xu FY, Jiang L, Cheng QF (2017) Superior fatigue resistant bioinspired graphene-based nanocomposite via synergistic interfacial interactions. *Adv Funct Mater* 27:1605636.
34. Hu K, et al. (2013) Written-in conductive patterns on robust graphene oxide biopaper by electrochemical microstamping. *Angew Chem Int Ed Engl* 52:13784–13788.
35. Ming P, et al. (2015) Nacre-inspired integrated nanocomposites with fire retardant properties by graphene oxide and montmorillonite. *J Mater Chem A* 3:21194–21200.
36. Wan S, et al. (2016) Nacre-inspired integrated strong and tough reduced graphene oxide-poly(acrylic acid) nanocomposites. *Nanoscale* 8:5649–5656.
37. Zhang Q, Wan SJ, Jiang L, Cheng QF (2017) Bioinspired robust nanocomposites of cooper ions and hydroxypropyl cellulose synergistic toughening graphene oxide. *Sci China Technol Sci* 60:758–764.
38. Cheng QF, et al. (2009) High mechanical performance composite conductor: Multi-walled carbon nanotube sheet/bismaleimide nanocomposites. *Adv Funct Mater* 19: 3219–3225.
39. Cheng Q, Li M, Jiang L, Tang Z (2012) Bioinspired layered composites based on flattened double-walled carbon nanotubes. *Adv Mater* 24:1838–1843.
40. Coleman JN, et al. (2003) Improving the mechanical properties of single-walled carbon nanotube sheets by intercalation of polymeric adhesives. *Appl Phys Lett* 82: 1682–1684.
41. Olek M, et al. (2004) Layer-by-layer assembled composites from multiwall carbon nanotubes with different morphologies. *Nano Lett* 4:1889–1895.
42. Li J, et al. (2011) High performance, freestanding and superthin carbon nanotube/epoxy nanocomposite films. *Nanoscale* 3:3731–3736.
43. Shin MK, et al. (2012) Synergistic toughening of composite fibres by self-alignment of reduced graphene oxide and carbon nanotubes. *Nat Commun* 3:650–657.
44. Jiang S, et al. (2017) Ultrastrong steel via minimal lattice misfit and high-density nanoprecipitation. *Nature* 544:460–464.
45. Wu G, Chan K-C, Zhu L, Sun L, Lu J (2017) Dual-phase nanostructuring as a route to high-strength magnesium alloys. *Nature* 545:80–83.
46. Ren ZJ, Xue GX (2007) *Practical Handbook for Metal Materials* (Jiangsu Science and Technology Press, Nanjing, China). Chinese.
47. Kim S-H, Kim H, Kim NJ (2015) Brittle intermetallic compound makes ultrastrong low-density steel with large ductility. *Nature* 518:77–79.
48. He BB, et al. (2017) High dislocation density-induced large ductility in deformed and partitioned steels. *Science* 357:1029–1032.
49. Melveger AJ, Baughman RH (1973) Raman spectral changes during the solid-state polymerization of diacetylenes. *J Polym Sci B Polym Phys* 11:603–619.
50. Barentsen HM, van Dijk M, Kimkes P, Zuilhof H, Sudhölter EJR (1999) Dye-substituted acetylenes and diacetylenes: Convenient polymerization as studied by differential scanning calorimetry, FT-IR, and UV-vis spectroscopy. *Macromolecules* 32:1753–1762.
51. Pei SF, Zhao JP, Du JH, Ren WC, Cheng HM (2010) Direct reduction of graphene oxide films into highly conductive and flexible graphene films by hydrohalic acids. *Carbon* 48:4466–4474.
52. Stankovich S, et al. (2007) Synthesis of graphene-based nanosheets via chemical reduction of exfoliated graphite oxide. *Carbon* 45:1558–1565.
53. Moon IK, Lee J, Ruoff RS, Lee H (2010) Reduced graphene oxide by chemical graphitization. *Nat Commun* 1:73.
54. Barthelat F, Yin Z, Buehler MJ (2016) Structure and mechanics of interfaces in biological materials. *Nat Rev Mater* 1:16007.
55. Zhu J, Zhang H, Kotov NA (2013) Thermodynamic and structural insights into nanocomposites engineering by comparing two materials assembly techniques for graphene. *ACS Nano* 7:4818–4829.
56. Shahzad F, et al. (2016) Electromagnetic interference shielding with 2D transition metal carbides (MXenes). *Science* 353:1137–1140.
57. Shen B, Zhai WT, Zheng WG (2014) Ultrathin flexible graphene film: An excellent thermal conducting material with efficient EMI shielding. *Adv Funct Mater* 24: 4542–4548.
58. Kumar P, et al. (2015) Large-area reduced graphene oxide thin film with excellent thermal conductivity and electromagnetic interference shielding effectiveness. *Carbon* 94:494–500.
59. Ye SB, Chen B, Hu DD, Liu CZ, Feng JC (2016) Graphene-based films with integrated strength and toughness via a novel two-step method combining gel casting and surface crosslinking. *ChemNanoMat* 2:816–821.
60. Mohiuddin TMG, et al. (2009) Uniaxial strain in graphene by Raman spectroscopy: *G* peak splitting, Grüneisen parameters, and sample orientation. *Phys Rev B* 79:205433.
61. Gao Y, et al. (2011) The effect of interlayer adhesion on the mechanical behaviors of macroscopic graphene oxide papers. *ACS Nano* 5:2134–2141.
62. Liu LQ, Barber AH, Nuriel S, Wagner HD (2005) Mechanical properties of functionalized single-walled carbon-nanotube/poly(vinyl alcohol) nanocomposites. *Adv Funct Mater* 15:975–980.
63. Lachman N, et al. (2009) Raman response of carbon nanotube/PVA fibers under strain. *J Phys Chem C* 113:4751–4754.
64. Mu M, Osswald S, Gogotsi Y, Winey KI (2009) An in situ Raman spectroscopy study of stress transfer between carbon nanotubes and polymer. *Nanotechnology* 20:335703.

Supporting Information

Sequentially bridged graphene sheets with high strength, toughness, and electrical conductivity

Sijie Wan[a,b,1], Yuchen Li[a,b,1], Jiuke Mu[c,1], Ali E. Aliev[c], Shaoli Fang[c], Nicholas A. Kotov[b,d,e], Lei Jiang[a,b], Qunfeng Cheng[a,b,2], Ray H. Baughman[c,2]

[a] Key Laboratory of Bio-inspired Smart Interfacial Science and Technology of Ministry of Education, School of Chemistry, Beihang University, Beijing 100191, P. R. China
[b] Beijing Advanced Innovation Center for Biomedical Engineering, Beihang University, Beijing 100191, P. R. China
[c] Alan G. MacDiarmid NanoTech Institute, University of Texas at Dallas, Richardson, TX 75080, USA
[d] Department of Chemical Engineering, University of Michigan, Ann Arbor, Michigan 48109, USA
[e] Biointerface Institute, University of Michigan, Ann Arbor, MI, 48109; USA

[1]S.W., Y.L., and J.M. contributed equally to this work.

[2]To whom correspondence should be addressed. Email: cheng@buaa.edu.cn or ray.baughman@utdallas.edu.

Materials and Methods

Fabrication of G-PCO, πBG, SBG sheets. The as-prepared GO was dispersed in DIW, to realize a concentration of 2 $mg \cdot mL^{-1}$, by continual stirring for 2 h and ultrasonication for 15 min. Then, 7-8 mL of GO dispersion was filtered under vacuum to make a freestanding GO sheet. After drying at 45 ℃ for 24 h, the GO sheet was soaked into pre-mixed THF/PCO solution (3 $mg \cdot mL^{-1}$) for 1 h, followed by UV irradiation at a wavelength of 254 nm for 2 h in N_2 atmosphere to form a GO-PCO sheet. Subsequently, the GO-PCO sheet was reduced to a G-PCO sheet by immersion in HI solution for 6 h, followed by washing five times with ethanol and drying at 45 ℃ for 2 h. Next, the G-PCO sheet was immersed into a pre-mixed DMF/PSE solution (24 $mmol \cdot L^{-1}$) to absorb PSE molecules, followed by rinsing five times with DMF and drying at 45 ℃ for 2 h. Finally, the SBG sheet was obtained by immersing into a pre-mixed DMF/AP solution (24 $mmol \cdot L^{-1}$) to absorb AP molecules, which can react with PSE molecules by nucleophilic acyl substitution of primary amine group, followed by rinsing five times with DMF and drying at 45 ℃ for 2 h. Based on the immersion time in AP and PSE solutions, five kinds of SBG sheets have been fabricated as follows: SBG-I (3 h), SBG-II (6 h), SBG-III (12 h), SBG-IV (24 h), and SBG-V (48 h). The corresponding πBG sheets were fabricated by eliminating treatment with PCO.

Characterization. Atomic force microscopy (AFM) images of GO nanosheets were obtained using a Leica TCS SP5 in the contact mode. Stress-strain curves were measured using a Shimadzu AGS-X Tester at a loading rate of 1 $mm \cdot min^{-1}$. A conventional frame-mounting method was used for mounting samples for stress-strain measurements. In our application of this method, the sample was adhesively attached to a paper frame that has a rectangular hole cut that is sufficiently wide and long to accommodate the samples width and gauge length. The sample length, gauge length, and width were 10, 5, and 3 mm, respectively. This rigid frame enabled the attachment of the sample to the testing apparatus without damage, and the subsequent cutting of the legs of the frame to release the sample for tensile tests. Fracture rarely occurred near the clamps. The thickness of each tested sample strip was obtained by averaging thickness values at 3 to 5 different positions, which was used to calculate the mechanical property of the corresponding sample strip. Then the average mechanical property for each sample type, and their standard deviations, were obtained from measured property values for 3 to 5 sample strips. To avoid uncertainties in the measurement of sample cross-sectional area, gravimetric strengths were obtained as the ratio of force at break to the sample weight per sample length. Dynamic tensile fatigue tests were conducted at a frequency of 1 Hz using an Instron ElectroPulsE1000 mechanical apparatus and a ratio of the minimum stress to maximum stress of 0.1. The samples used for fatigue testing were 25-mm-long, 5-mm-wide strips. TGA curves were recorded under nitrogen atmosphere on a TG/DTA6300 (NSK, Japan) using a temperature increase rate of 10 $ºC \cdot min^{-1}$ from room temperature to 800 ºC. SEM images were

obtained by field-emission scanning electron microscopy (JEOL-7500F) at an acceleration voltage of 5 kV. Raman spectra were recorded on a LabRAM HR800 (Horiba Jobin Yvon) using 633 nm excitation. The laser power was kept below 0.5 mW to avoid laser heating. For the Raman mapping over a 400 μm^2 square area under different applied strains, Raman spectra were recorded with the step size of 500 nm. All G bands in the Raman spectra were fitted with Lorentzian functions to obtain peak positions. XRD curves were measured on a Shimadzu XRD-6000 using Cu-Kα radiation and a scanning speed of $4^{o} \cdot min^{-1}$. WAXS measurements were carried out at NCD beamline11 (ALBA Synchrotron Light Facility, Spain) with the distance between sample and detector CCD of 20 cm. XPS measurements were performed on an ESCALab220i-XL (ThermoScientific) using a monochromatic Al-Kα X-ray source. FTIR spectra were carried out using a Thermo Nicolet NEXUS-470 FTIR instrument in the attenuated total reflection mode. UV-vis spectra were obtained using a Lambda750 spectrophotometer. Electrical conductivities were measured using a four-probe method on an electrical transport properties measurement system (Keithley 2400 multiple-function source-meter). Gravimetric electrical conductivities were obtained by dividing the inverse electrical resistance per sample length by the sample weight per sample length in the electrical conductivity direction. EMI shielding effectiveness measurements were carried out using an AV3629 vector network analyzer in the frequency range between 0.3 and 12 GHz.

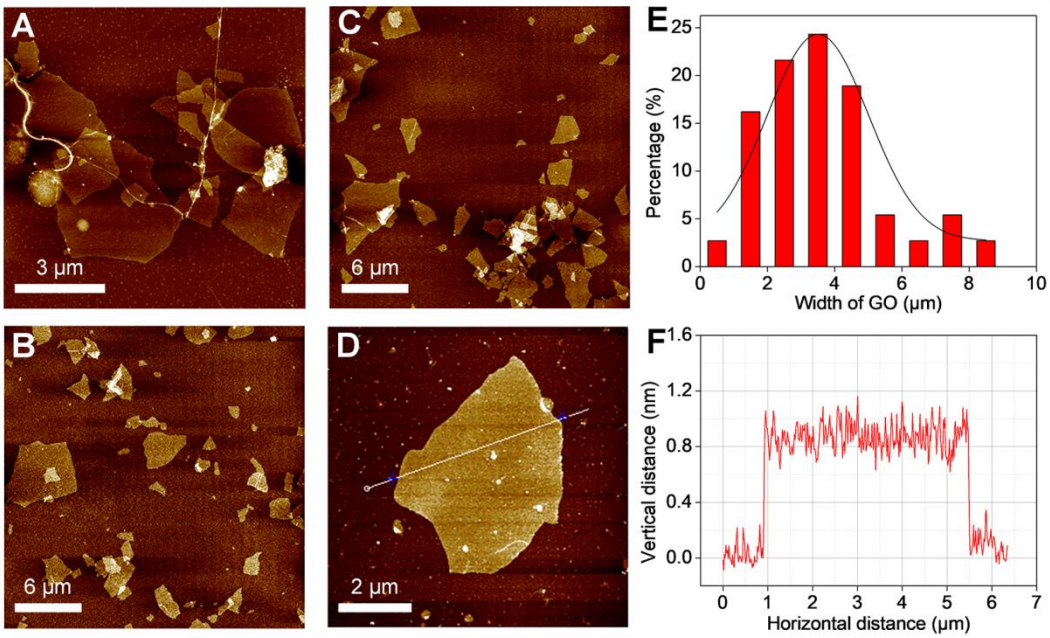

Fig. S1. Atomic force microscopy (AFM) characterization of exfoliated graphene oxide (GO) nanosheets. (A to D) AFM images of GO nanosheets. (E) The width distribution of GO nanosheets, showing that the average width of GO nanosheets is about 3.5 μm. (F) The height profile of GO nanosheets in (D), showing that the thickness of GO nanosheets is about 0.8 nm.

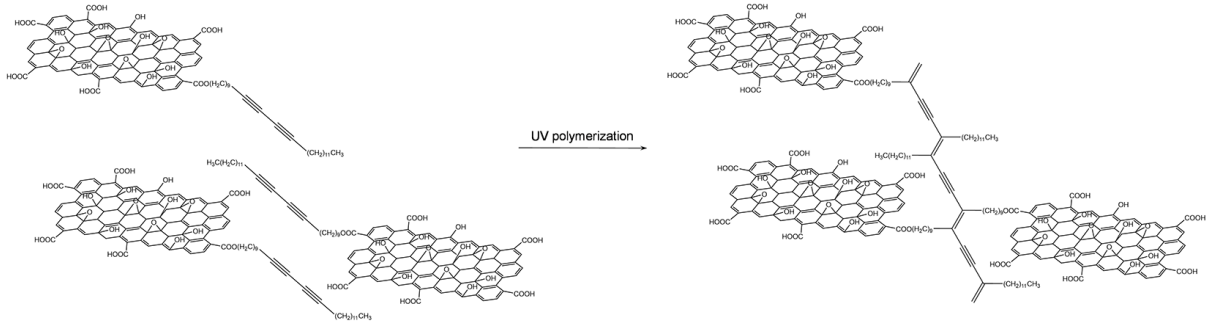

Fig. S2. (Left) Schematic illustration of an array of 10,12-pentacosadiyn-1-ol (PCO, $CH_3(CH_2)_{11}C \equiv C{-}C \equiv C(CH_2)_8CH_2OH$) molecules, whose OH groups have reacted with carboxyl groups on graphene oxide platelets. (Right) the 1,4-addition polymer formed by ultraviolet radiation of the monomer array on the left, thereby covalently connecting graphene oxide platelets. These illustrations are simplistic in that they only consider the possible function of the polydiacetylene bonding agent to reinforce the connectivity between the edges of adjacent platelets of graphene sheet stacks, and perhaps to indirectly provide enhanced bonding between graphene sheets in an individual stack. Both π-π bonding and covalent bonding between the platelet basal plane surfaces might also be especially important, and in the latter case approximately planar basal platelet planes can assist the organization of diacetylene molecules for topochemical polymerization.

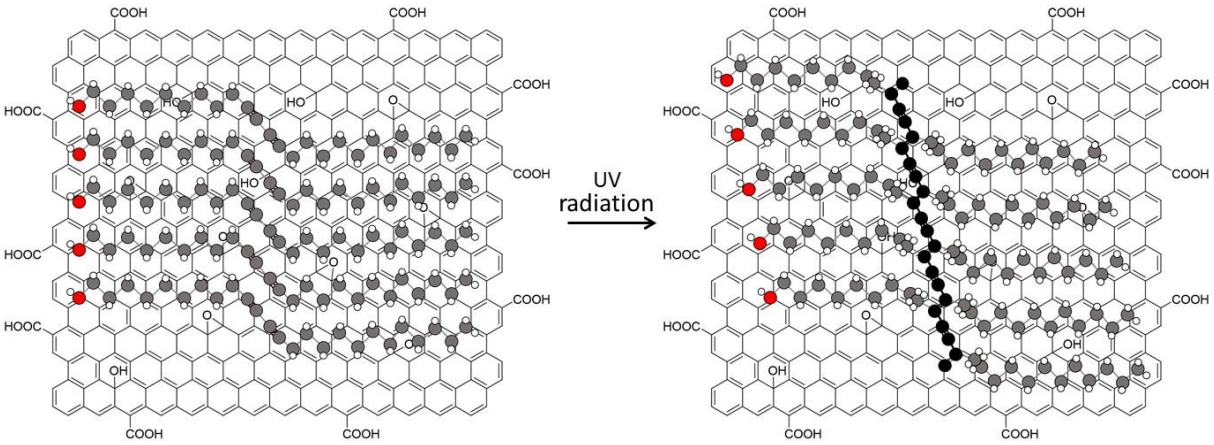

Fig. S3. Schematic illustration of the expected self-assembly of 10,12-pentacosadiyn-1-ol (PCO) molecules on the external basal-plane surface of graphene oxide platelet (left) and their polymerization by 1,4-addition polymerization to form polydiacetylene chains (right). The white spheres, red spheres, and grey spheres in the monomer array illustration represent hydrogen, oxygen, and carbon atoms, respectively. For the polymer chain, the black spheres denote carbon atoms in the polydiacetylene backbone. The observed shift in C≡C Raman vibration frequency and the observation of a long wavelength absorption due to long conjugated polydiacetylene chains confirm this polymerization. Both results were obtained for incident light normal to the sheet plane, which would maximize the intensity of both the C≡C Raman vibration and the long wavelength absorption. Based on previous scanning tunneling microscopy on graphite-substrate-supported PCO (20) and atomic force microscopy on graphite-substrate-supported 10,12-pentacosadiynoic acid (S1), arrays like pictured above are expected to be assembled in crystalline domains (having largely random orientations) on the graphene oxide (GO) surface. The carbon atoms in the polydiacetylene chain are above the graphene substrate, since these investigations show that this minimizes the atom displacements needed for 1,4-addition polymerization. While neighboring monomer arrays dimerize by hydrogen bonding on graphite, the oxygen functionalities on the GO might partially disrupt this dimerization.

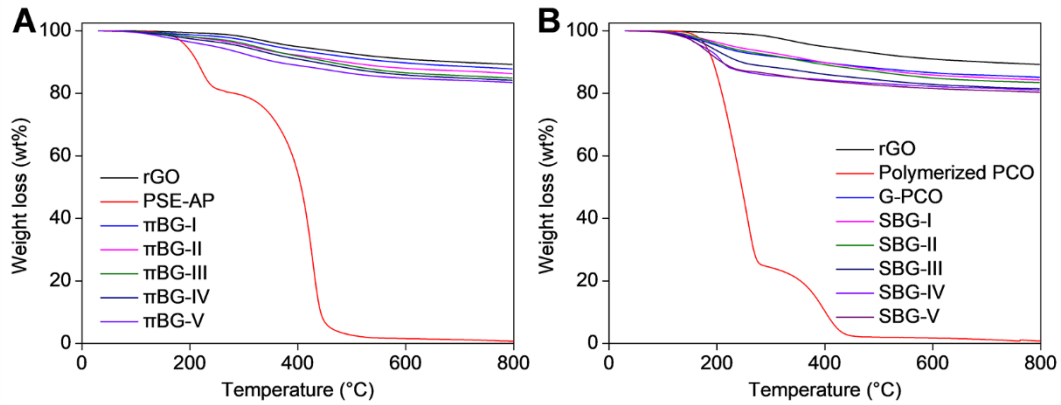

Fig. S4. Thermogravimetric analysis (TGA) curves. (A) 1-pyrenebutyric acid N-hydroxysuccinimide ester and 1-aminopyrene (PSE-AP), reduced graphene oxide (rGO), and π-bridged graphene (πBG) sheets. (B) Polymerized PCO, rGO, G-PCO, and sequentially bridged graphene (SBG) sheets. The TGA measurements were conducted under nitrogen atmosphere from room temperature to 800 ºC using a temperature increase rate of 10 ºC/min.

The weight fraction of PSE-AP in πBG sheets was estimated from the weight loss curve over the temperature range from 100 ºC to 800 ºC. The PSE-AP weight fraction (w_1) in πBG sheets is approximately given by equation 1,

$$w_1 = \frac{M_{\pi BG} - M_{rGO}}{0.992 - M_{rGO}} \quad (1)$$

where 0.992, M_{rGO} and $M_{\pi BG}$ are the fraction of weight loss for PSE-AP, rGO, and πBG sheets, respectively, between 100℃ and 800℃.

The weight fraction (w_2) of PCO in sheets of G-PCO and the weight fraction (w_3) of PSE-AP in SBG sheets were analogously obtained. Since the PCO/rGO weight ratio in SBG should be the same as in G-PCO, the weight fraction (w_4) of PCO in SBG sheets should be approximately given by equation 2:

$$w_4 = (1-w_3) \times w_2 \quad (2)$$

The detailed data for PCO and PSE-AP weight percentage in G-PCO, πBG, and SBG sheets are tabulated in Table S2.

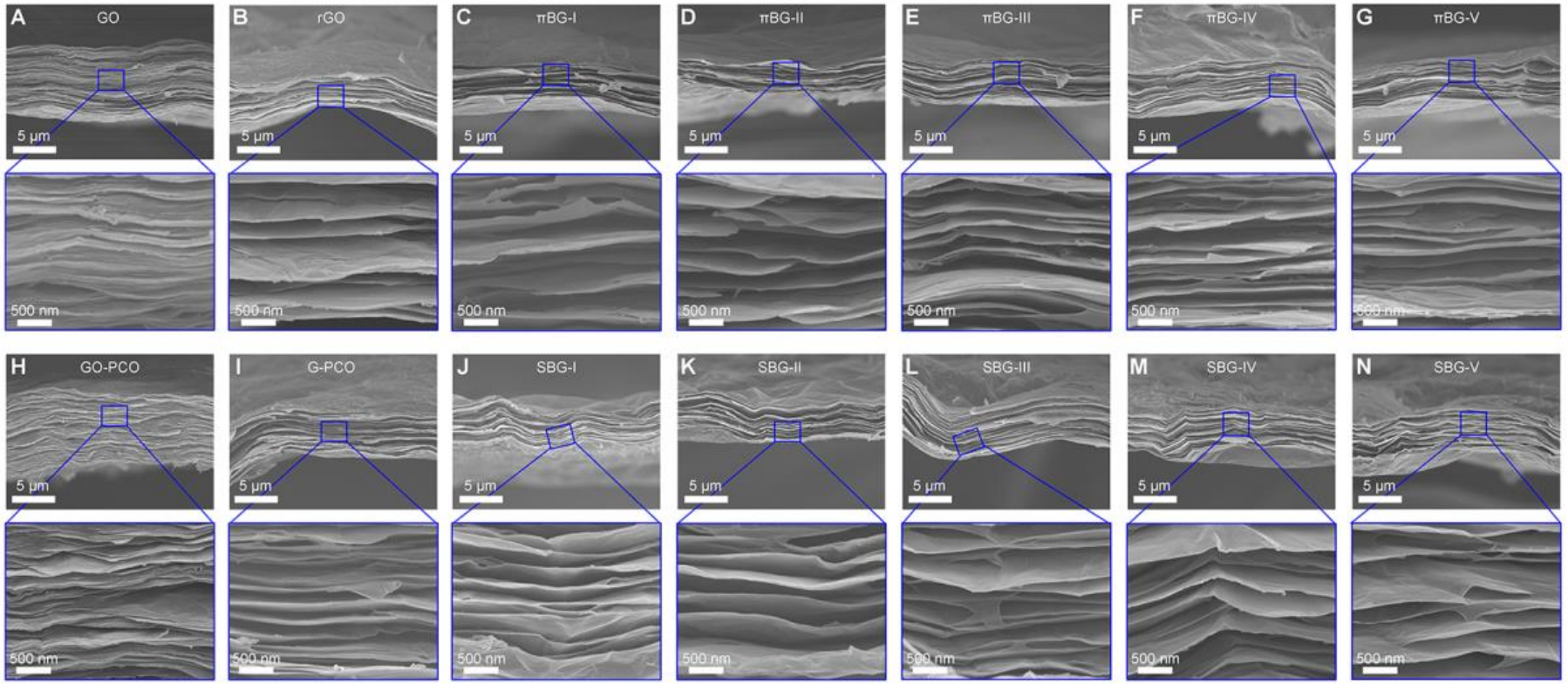

Fig. S5. Scanning electron microscope (SEM) images of sheet edges resulting from sheet fracture. (A) GO, (B) rGO, (C to G) πBG-I to πBG-V, (H) GO-PCO, (I) G-PCO, and (J to N) SBG-I to SBG-V sheets. These images show the layered structures of the sheets.

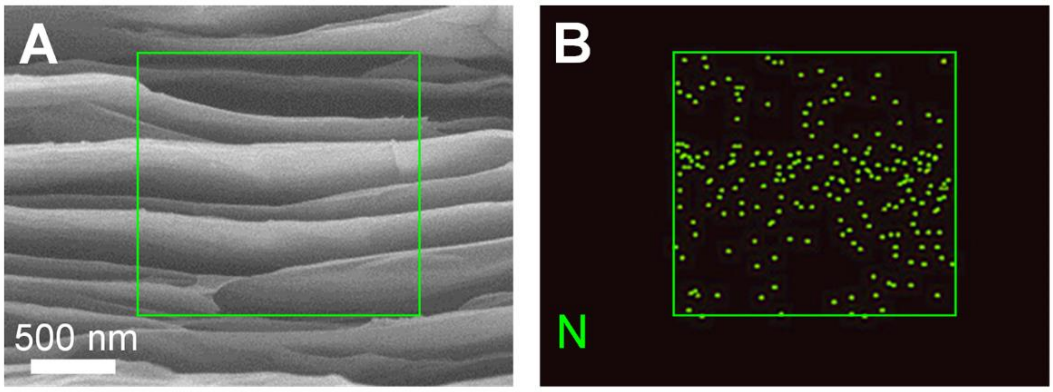

Fig. S6. (A) SEM image of cross section and (B) corresponding energy dispersive X-ray spectroscopy (EDS) mapping of nitrogen for SBG-V sheets.

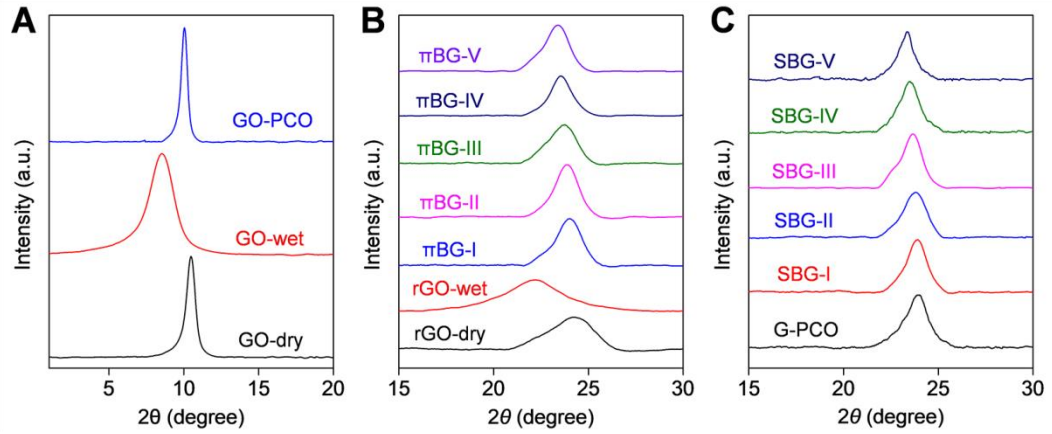

Fig. S7. X-ray diffraction (XRD) patterns using Cu-Kα radiation. (A) dry GO, wet GO (immersed in tetrahydrofuran (THF) for 1 h), and dry GO-PCO sheets. (B) dry rGO, wet rGO (immersed in N, N-dimethylformamide (DMF) for 48 h) and dry πBG sheets. (C) dry G-PCO and SBG sheets. The wet GO and rGO sheets show larger interlayer diffraction spacing than do dry GO and rGO sheets, indicating that the layers of GO and rGO sheets are separating during immersion in THF and DMF. Such separation enhances the insertion of PCO, PSE, and AP molecules into wet GO and rGO. Note that the interlayer diffraction spacings of dry G-PCO, πBG, and SBG sheets are larger than for dry rGO sheets.

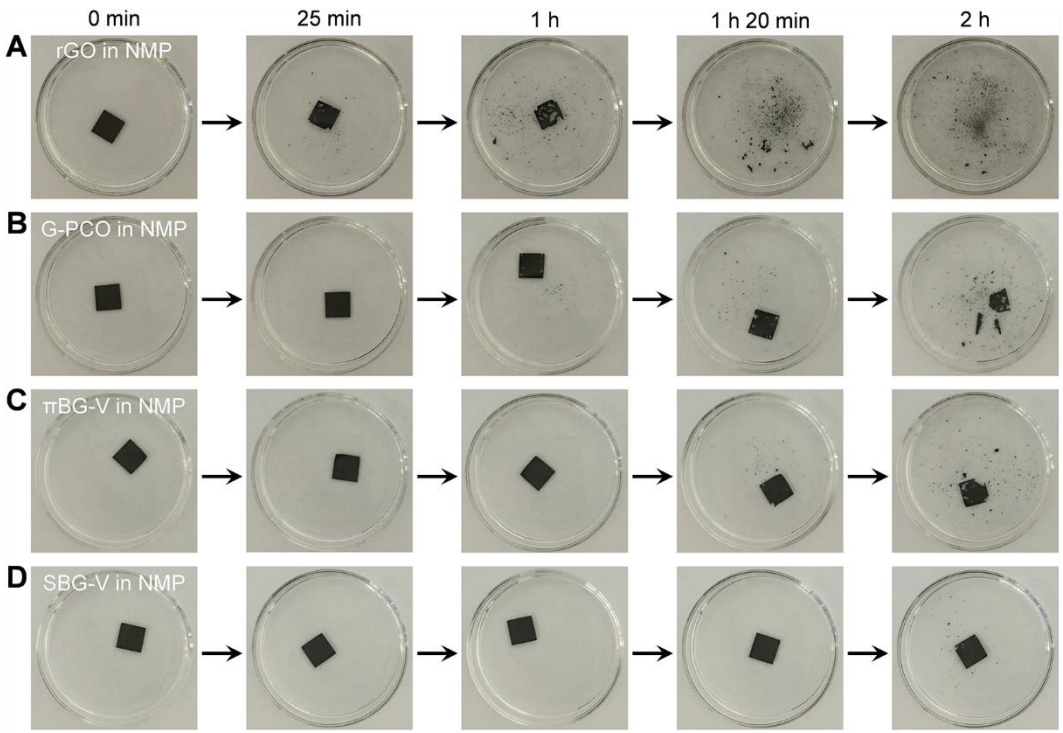

Fig. S8. Photographs of sheets during ultrasonication (using a 100 W, 40 kHz sonicator) in N-methyl-2-pyrrolidone (NMP). The (A) rGO, (B) G-PCO, (C) πBG-V, and (D) SBG-V sheets begin to disintegrate after ultrasonication for 25 min, 1 h, 1 h 20 min, and 2 h, respectively, indicating the increased resistance to disintegration of the bridged graphene sheets.

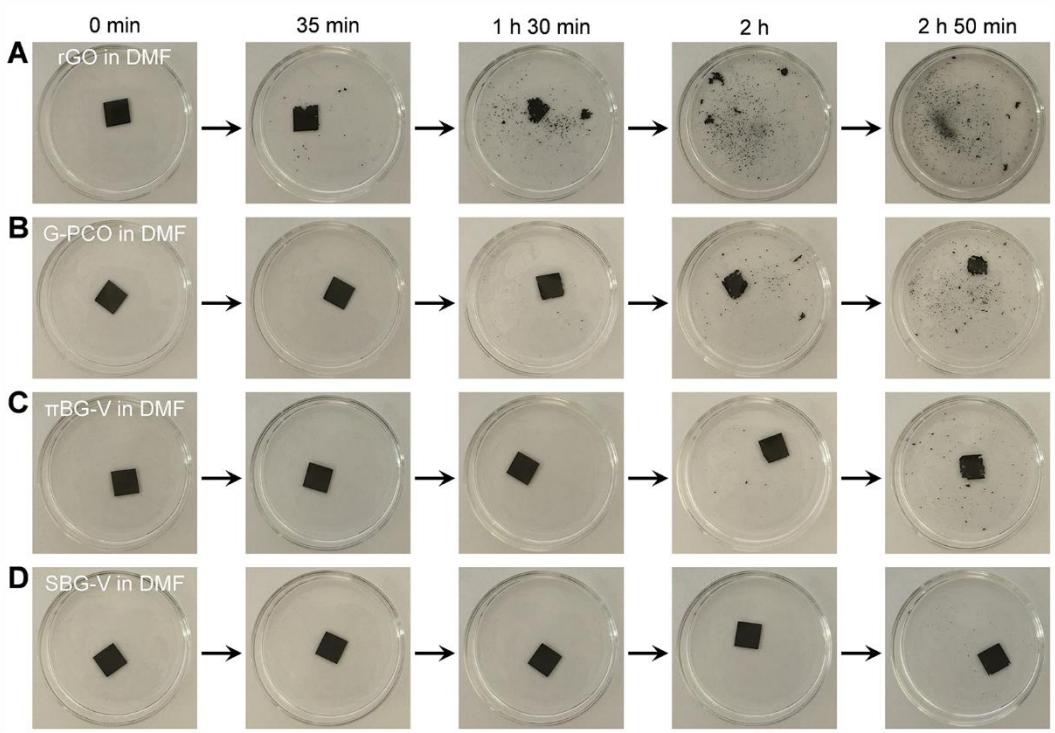

Fig. S9. Photographs of sheets during ultrasonication (using a 100 W, 40 kHz sonicator) in DMF. The (A) rGO, (B) G-PCO, (C) πBG-V, and (D) SBG-V sheets begin to disintegrate after ultrasonication for 35 min, 1 h 30 min, 2 h, and 2 h 50 min, respectively, indicating the increased resistance to disintegration of the bridged graphene sheets.

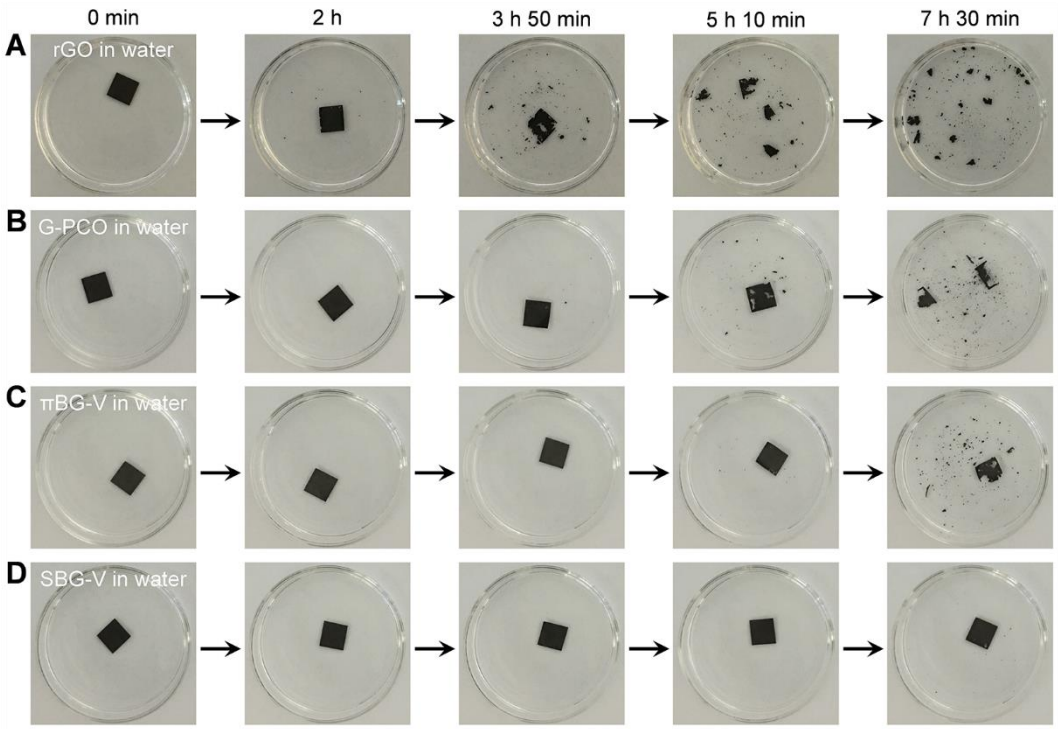

Fig. S10. Photographs of sheets during ultrasonication (using a 100 W, 40 kHz sonicator) in water. The (A) rGO, (B) G-PCO, (C) πBG-V, and (D) SBG-V sheets begin to disintegrate after ultrasonication for 2 h, 3 h 50 min, 5 h 10 min, and 7 h 30 min, respectively, indicating the increased resistance to disintegration of the bridged graphene sheets.

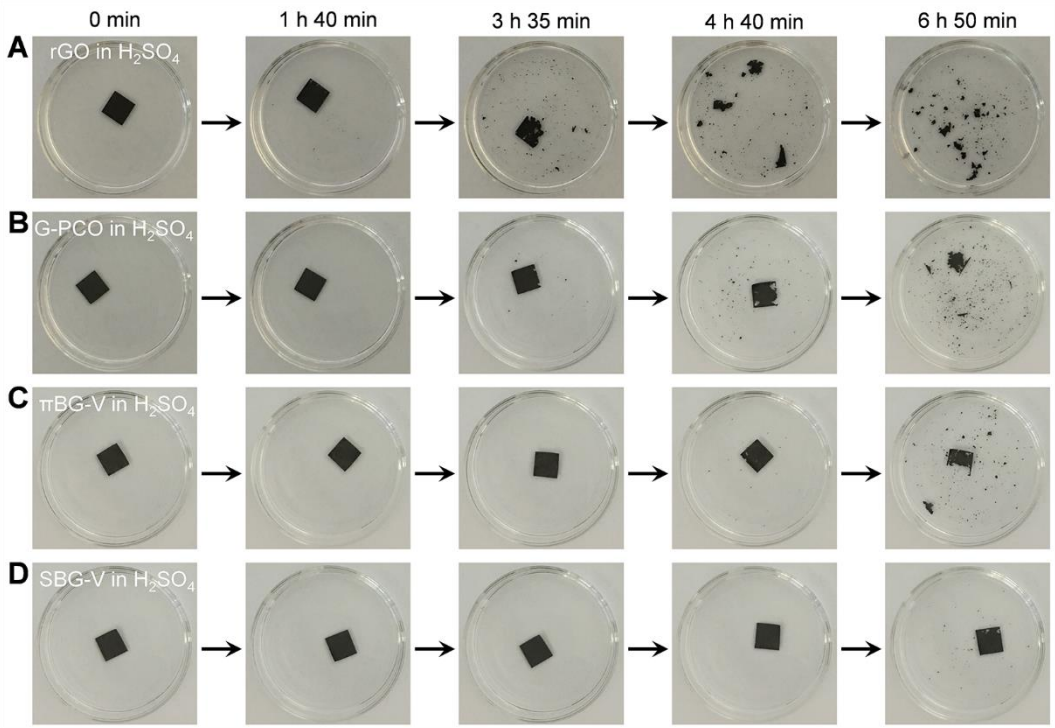

Fig. S11. Photographs of sheets during ultrasonication (using a 100 W, 40 kHz sonicator) in sulfuric acid (H_2SO_4) solution (with H^+ concentration of 8 mol·L^{-1}). The (A) rGO, (B) G-PCO, (C) πBG-V, and (D) SBG-V sheets begin to disintegrate after ultrasonication for 1 h 40 min, 3 h 35 min, 4 h 40 min, and 6 h 50 min, respectively, indicating the increased resistance to disintegration of the bridged graphene sheets.

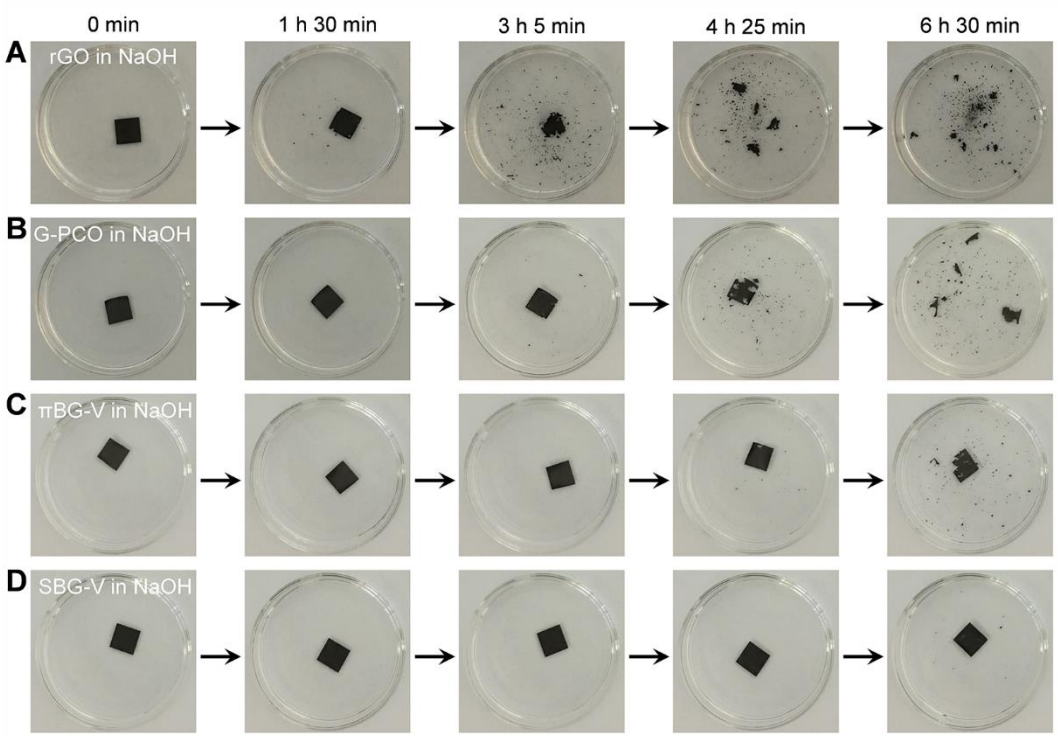

Fig. S12. Photographs of sheets during ultrasonication (using a 100 W, 40 kHz sonicator) in sodium hydroxide (NaOH) solution (with OH^- concentration of 8 $mol \cdot L^{-1}$). The (A) rGO, (B) G-PCO, (C) πBG-V, and (D) SBG-V sheets begin to disintegrate after ultrasonication for 1 h 30 min, 3 h 5 min, 4 h 25 min, and 6 h 30 min, respectively, indicating the increased resistance to disintegration of the bridged graphene sheets.

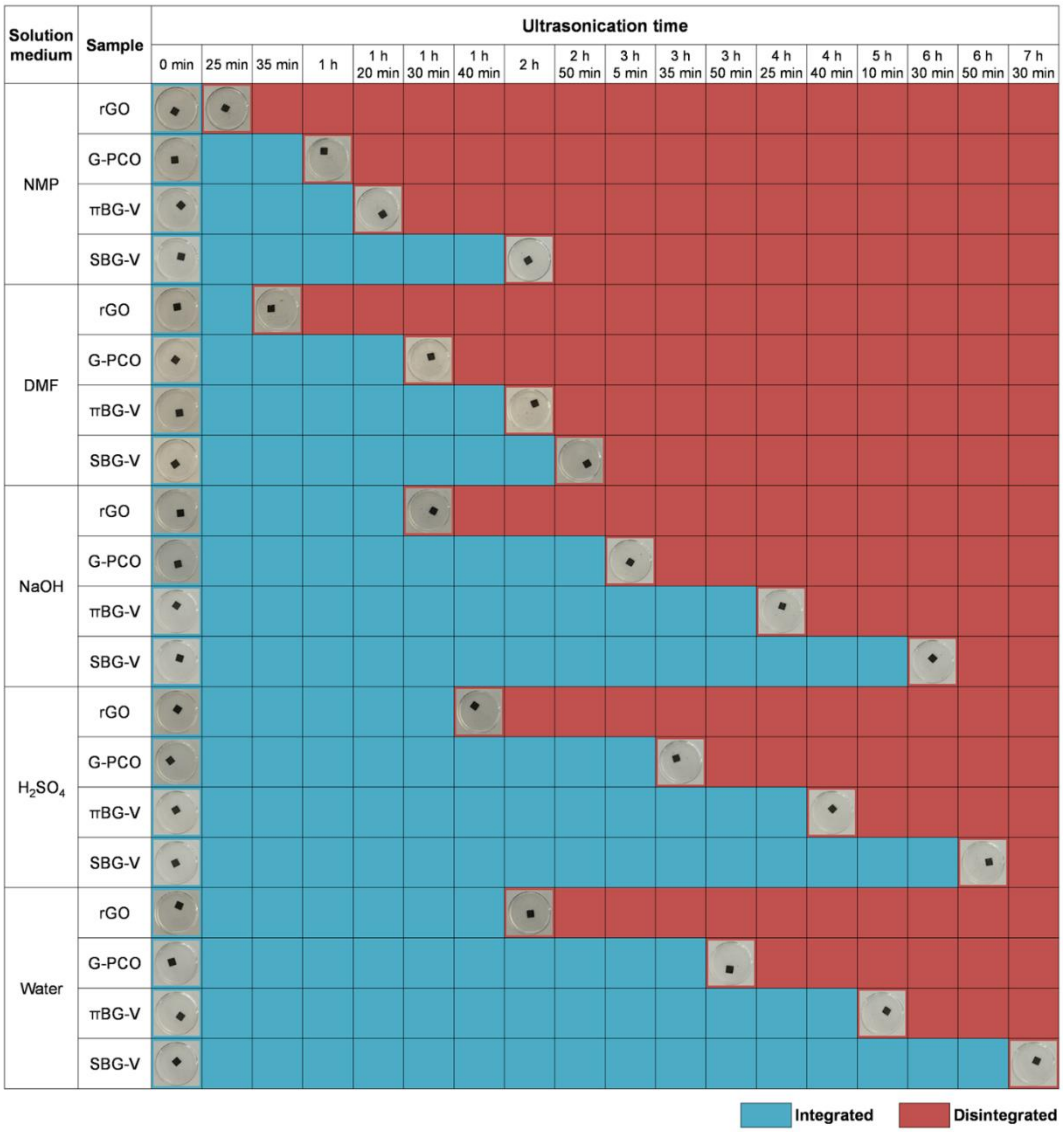

Fig. S13. The integrity of SBG sheets during ultrasonication (100 W, 40 kHz) for different times in NMP, DMF, water, H_2SO_4 (with H^+ concentration of 8 $mol \cdot L^{-1}$), NaOH (with OH^- concentration of 8 $mol \cdot L^{-1}$) solutions. The resistance to disintegration of sheet structure under ultrasonication in all liquids increases in going from rGO, G-PCO, and πBG-V to SBG-V.

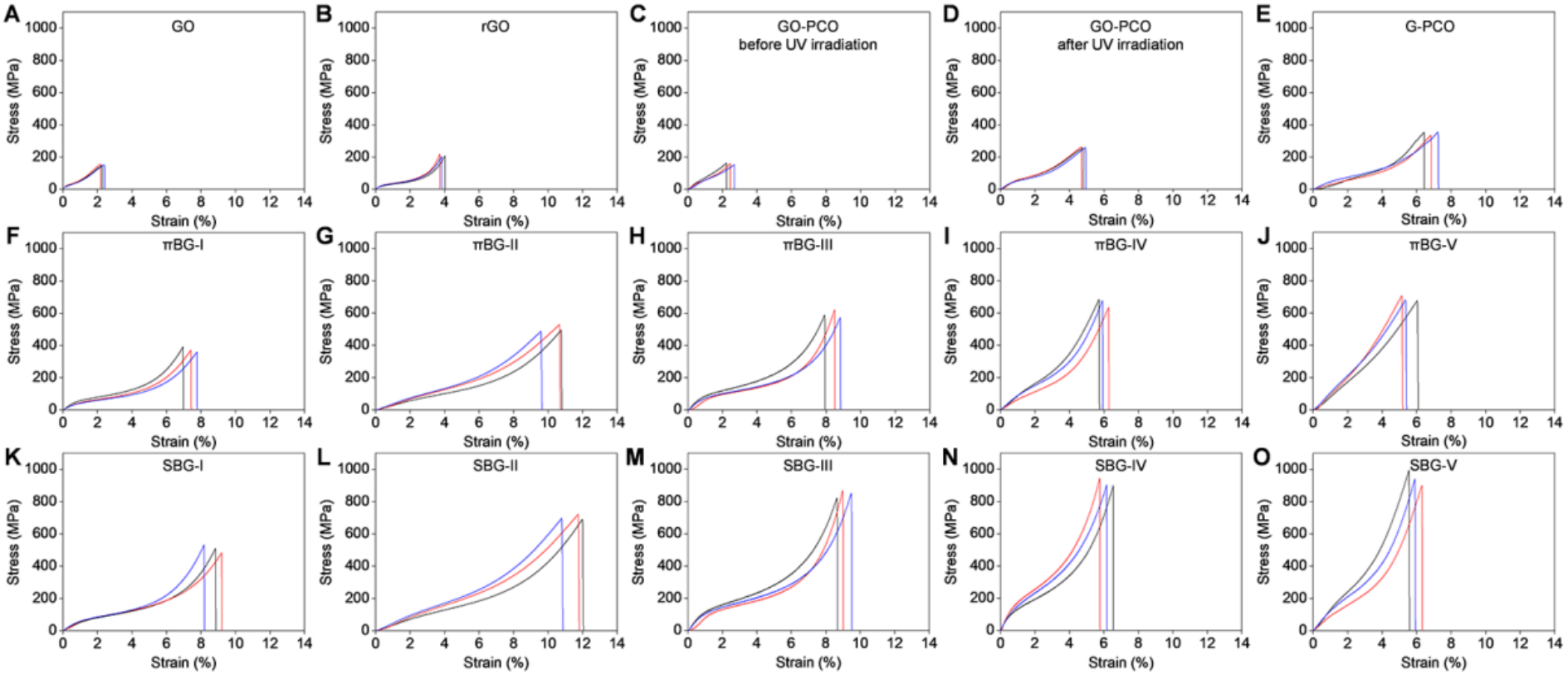

Fig. S14. Tensile stress-strain curves of sheets. (A) GO, (B) rGO, (C) GO-PCO before ultraviolet (UV) irradiation, (D) GO-PCO after UV irradiation, (E) G-PCO, (F to J) πBG-I to πBG-V, and (K to O) SBG-I to SBG-V.

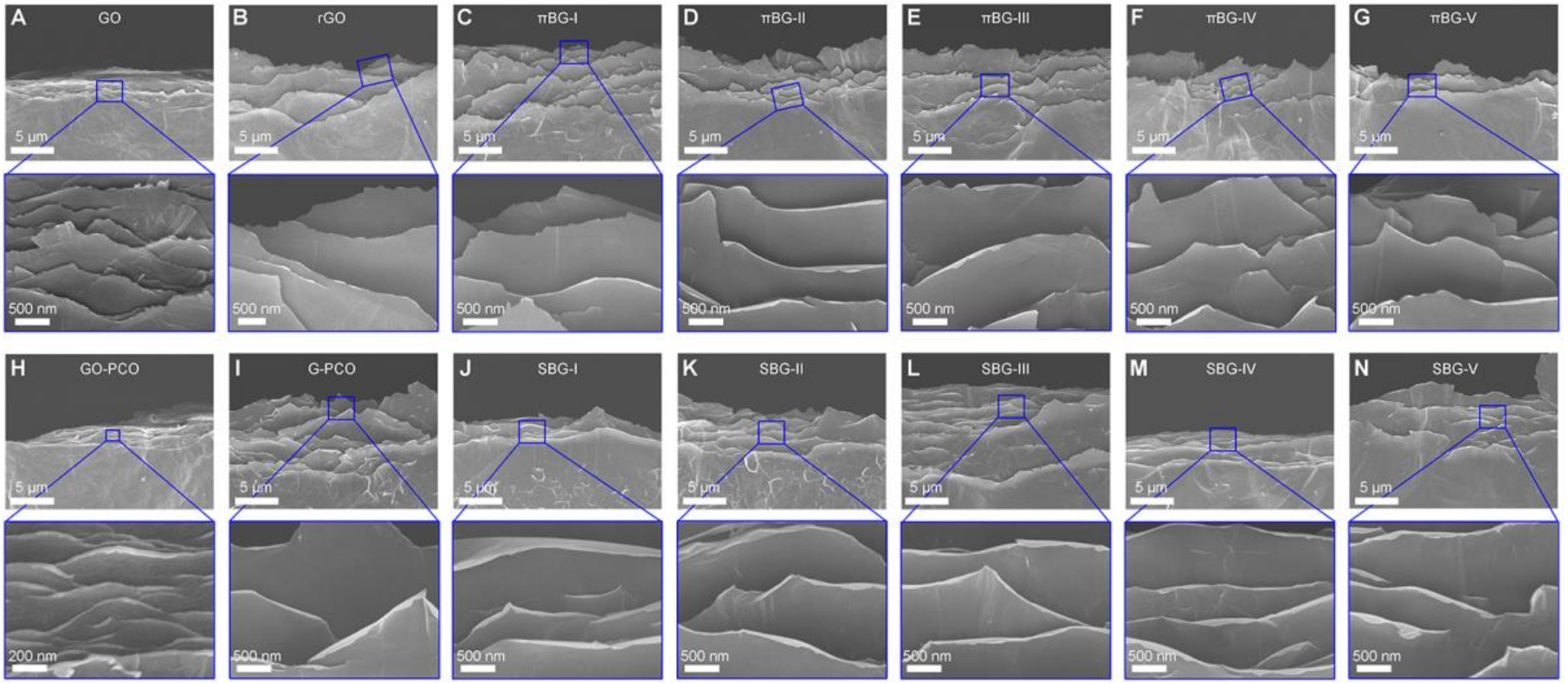

Fig. S15. Inclined-view SEM images of sheet edges resulting from sheet fracture. (A) GO, (B) rGO, (C to G) πBG-I to πBG-V, (H) GO-PCO, (I) G-PCO, and (J to N) SBG-I to SBG-V sheets. The bridged graphene sheets, including G-PCO, πBG, and SBG, curl at the fracture edge, which is not the case for the rGO sheets.

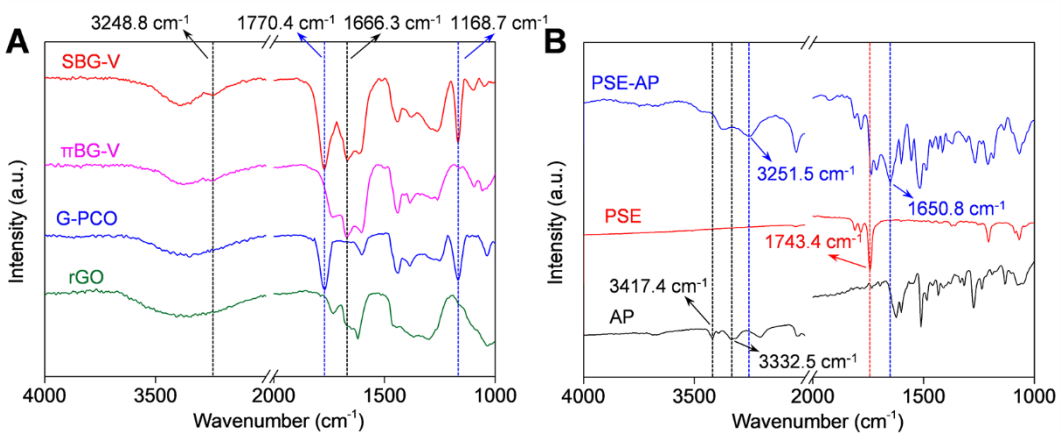

Fig. S16. Fourier transform infrared (FTIR) spectra. (A) rGO, G-PCO, πBG-V, and SBG-V sheets. (B) AP, PSE, and PSE-AP molecules. The peaks around 3251.5 cm^{-1} and 1650.8 cm^{-1} in PSE-AP correspond to the stretching vibrations of C=O and N−H, respectively, of amide groups. Thus, the peaks around 3248.8 cm^{-1} and 1666.3 cm^{-1} in πBG-V and SBG-V sheets indicate that the PSE and AP absorbed in these graphene structures have reacted to form amide linkages. The peaks around 1770.4 cm^{-1} and 1168.7 cm^{-1} in G-PCO are assigned to the stretching vibration of C=O and −C−O−C− of ester groups, demonstrating the reaction of the −OH groups of the PCO with −COOH groups of the GO nanosheets.

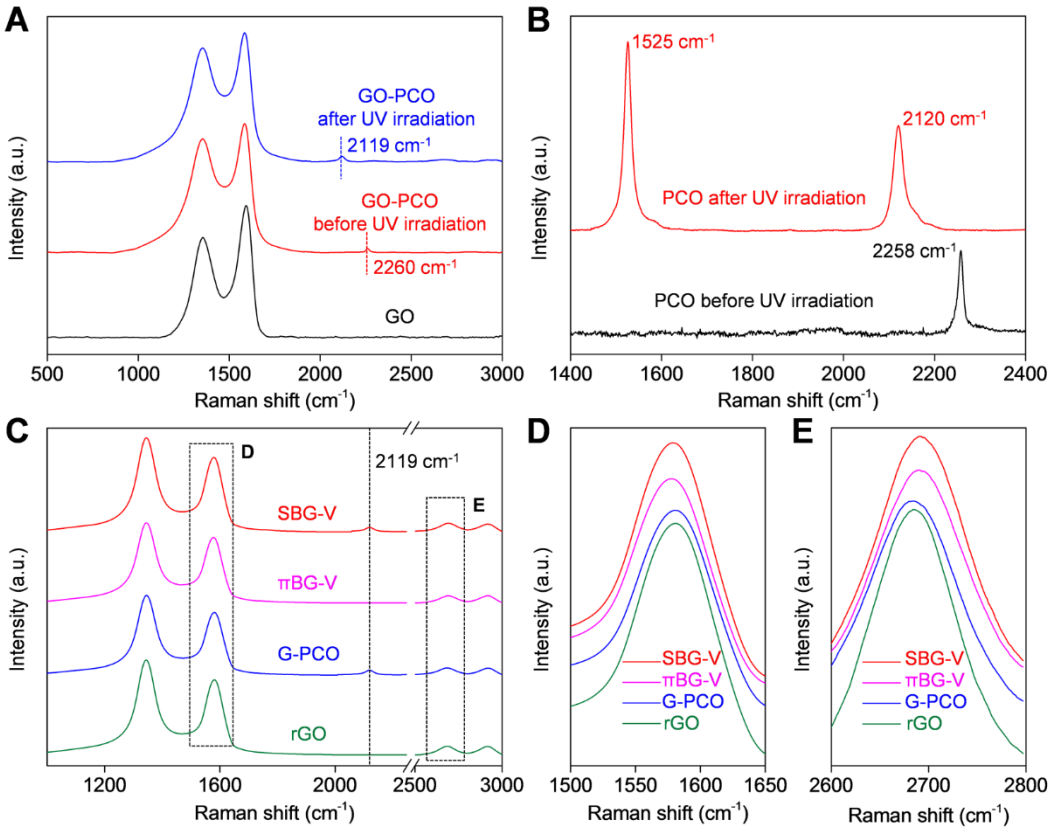

Fig. S17. Raman spectra for 633 nm excitation. (A) GO and GO-PCO sheets before and after UV irradiation (254 nm). (B) PCO before and after UV irradiation. (C) rGO, G-PCO, πBG-V, and SBG-V sheets. High resolution plots of the Raman spectra shown in (C) for Raman shift ranges of (D) 1500 to 1650 cm^{-1} and (E) 2600 to 2800 cm^{-1}. After UV irradiation, the C≡C vibration of neat PCO is down-shifted from 2258 cm^{-1} to 2120 cm^{-1} and a new peak, corresponding to the C=C vibration, appears at 1525 cm^{-1}, demonstrating the 1,4-addition polymerization of PCO. Since the PCO content in the PCO bridged sheets is relatively low, (~3.98 to ~4.21 wt%) the C=C vibration signal is so weak that it is overwhelmed by the strong G band of graphene sheets. The peak at 2119 cm^{-1} for G-PCO and SBG indicates that polymerized PCO exist in these sheets. Additionally, the G band frequency of πBG-V and SBG-V (~1578 cm^{-1}) is slightly down-shifted compared with that of rGO and G-PCO (~1581 cm^{-1}), while the 2D band frequency of πBG-V and SBG-V (~2690 cm^{-1}) is slightly up-shifted compared with that of rGO and G-PCO (~2684 cm^{-1}). The πBG-V and SBG-V sheets show similar *D/G* ratio to rGO and G-PCO sheets, respectively, as tabulated in Table S7, indicating that bridging introduces negligible disorder.

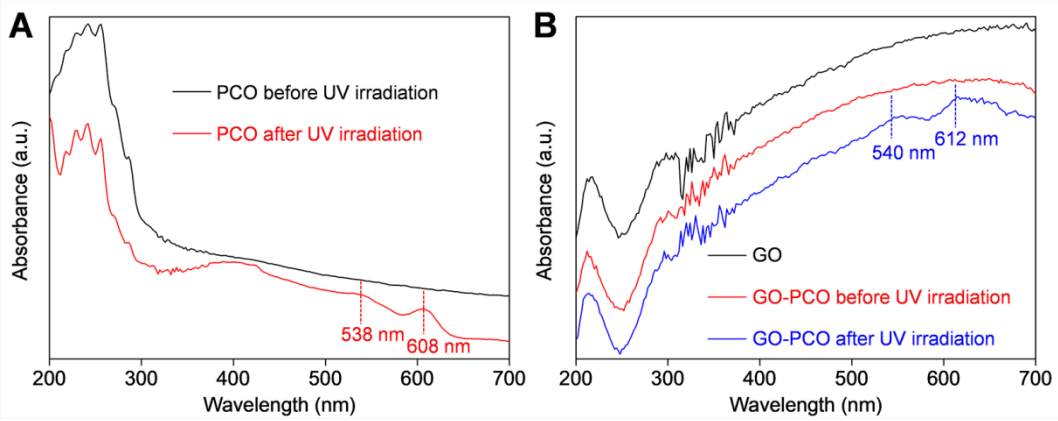

Fig. S18. Ultraviolet-visible (UV-vis) spectra. (A) PCO before and after UV irradiation. (B) GO and GO-PCO sheets before and after UV irradiation. After UV irradiation, the PCO and GO-PCO sheets show absorption peaks at 538 nm and 608 nm and at 540 nm and 612 nm, respectively, demonstrating the occurrence of the same polymerization reaction of neat PCO and GO-PCO.

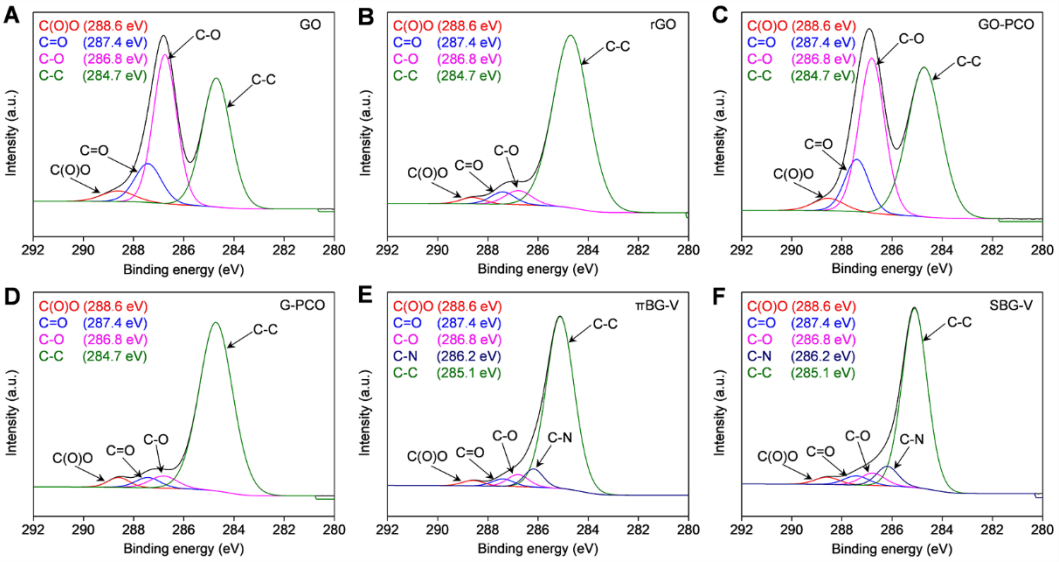

Fig. S19. X-ray photoelectron spectroscopy (XPS) for carbon. (A) GO, (B) rGO, (C) GO-PCO, (D) G-PCO, (E) πBG-V, and (F) SBG-V sheets. The broad C_{1s} peak of GO, rGO, GO-PCO, and G-PCO sheets can be fitted by four peaks at 288.6, 287.4, 286.8, and 284.7 eV, corresponding to C(O)O, C=O, C−O, and C(sp^2)−C(sp^2), respectively. The broad C_{1s} peak of πBG-V and SBG-V sheets can be fitted by five peaks at 288.6, 287.4, 286.8, 286.2, and 285.1 eV, corresponding to C(O)O, C=O, C−O, C−N, and C(sp^2)−C(sp^2), respectively. The new peak at 286.2 eV for πBG-V and SBG-V sheets is assigned to the C−N in amide groups, demonstrating the reaction between PSE and AP. Additionally, the C(sp^2)−C(sp^2) peak of πBG-V and SBG-V sheets (285.1 eV) is slightly up-shifted compared with that of GO, rGO, GO-PCO, and G-PCO sheets (284.7 eV). Furthermore, the O_{1s}/C_{1s} ratio of rGO (0.19), G-PCO (0.16), πBG-V (0.17), and SBG-V (0.16) is significantly decreased compared with that of GO (0.45) and GO-PCO (0.41), as tabulated in Table S8, indicating the substantial elimination of oxygen-containing groups of GO sheets by HI.

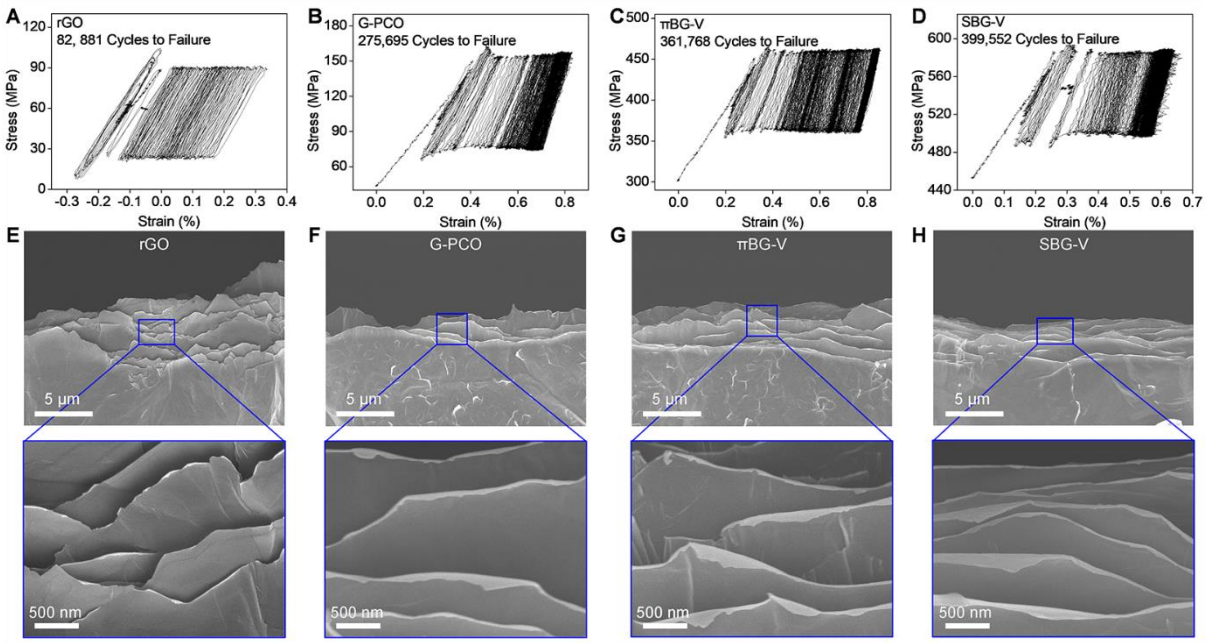

Fig. S20. Dynamic tensile stress-strain curves and corresponding fracture morphologies after tensile fatigue testing. (A and E) rGO, (B and F) G-PCO, (C and G) πBG-V, and (D and H) SBG-V sheets. The bridged graphene sheets demonstrate higher fatigue life and increased curling of fracture layer edges than rGO sheets.

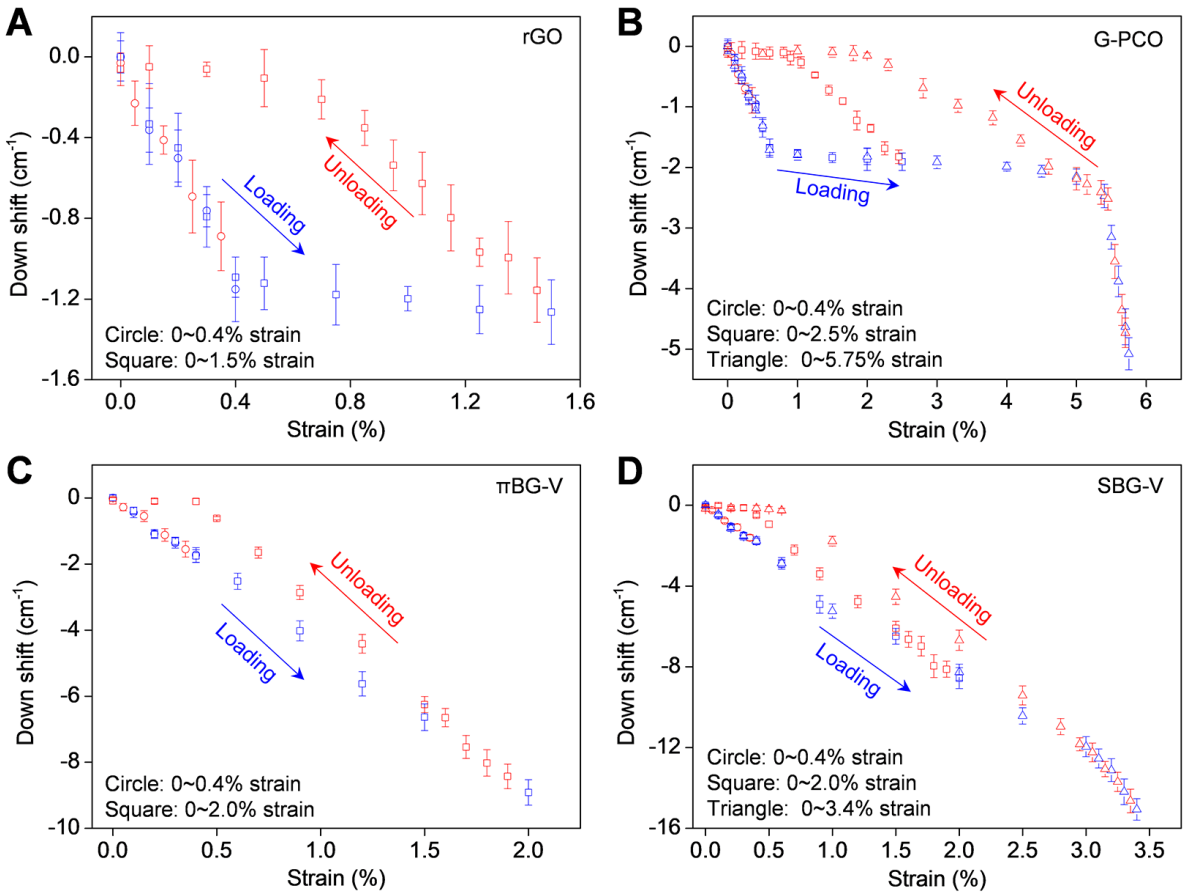

Fig. S21. Raman frequency shifts during loading/unloading processes. (A) rGO, (B) G-PCO, (C) πBG-V, and (D) SBG-V sheets. The Raman frequency shifts are reversible for these materials only when the maximum applied strain is below about 0.4%.

Table S1. The interlayer diffraction spacings of dry and wet GO, dry and wet rGO, and dry GO-PCO, G-PCO, πBG, and SBG sheets. The GO was wet by immersion in THF for 1 h and the rGO was wet by immersion in DMF for 48 h.

Sample	*d* (Å)
GO-dry	8.44
GO-wet	10.35
rGO-dry	3.66
rGO-wet	3.99
GO-PCO	8.81
G-PCO	3.72
πBG-I	3.70
πBG-II	3.72
πBG-III	3.75
πBG-IV	3.78
πBG-V	3.80
SBG-I	3.72
SBG-II	3.74
SBG-III	3.76
SBG-IV	3.79
SBG-V	3.81

Table S2. PCO and PSE-AP content of G-PCO, πBG, and SBG sheets.

Sample	PCO content (wt%) by TGA	PSE-AP content (wt%) by TGA
G-PCO	4.21	-
πBG-I	-	1.34
πBG-II	-	2.97
πBG-III	-	4.56
πBG-IV	-	5.31
πBG-V	-	5.92
SBG-I	4.17	0.94
SBG-II	4.12	2.21
SBG-III	4.03	4.32
SBG-IV	4.00	4.96
SBG-V	3.98	5.43

Table S3. The full width at half maximum (FWHM) of X-ray scattering intensity as a function of the azimuthal angle, and thereby the derived degree of graphene platelet orientation in rGO, G-PCO, πBG-V, and SBG-V sheets.

Sample	FWHM (°)	Degree of orientation (%)
rGO	41.8	76.8
G-PCO	28.7	84.1
πBG-V	25.1	86.1
SBG-V	24.5	86.4

The degree of graphene platelet orientation (Φ) was calculated using the following equation 3:

$$\Phi = \frac{180 - FWHM}{180} \times 100\% \quad (3)$$

Table S4. The tensile strength, toughness, electrical conductivity, density, gravimetric electrical conductivity, and electromagnetic interference (EMI) shielding effectiveness in the frequency range between 0.3 and 12 GHz for rGO, G-PCO, πBG-V, and SBG-V sheets. The gravimetric electrical conductivity was calculated by dividing the inverse electrical resistance per sample length by the weight per sample length in the electrical conductivity direction. Reflecting the accuracy of the density measurements for these thin sheets, nearly the same gravimetric electrical conductivity was obtained by dividing the electrical conductivity by the sample density.

Sample	Tensile strength (MPa)	Toughness (MJ/m^3)	Electrical conductivity ($S \cdot cm^{-1}$)	Density ($g \cdot cm^{-3}$)	Gravimetric electrical conductivity ($S \cdot cm^2 \cdot g^{-1}$)	EMI shielding effectiveness in the frequency range between 0.3 and 12 GHz (dB)
rGO	209.7 ± 8.0	2.6 ± 0.1	186.8 ± 16.9	2.01	92.9 ± 8.4	~11
G-PCO	348.5 ± 12.0	8.5 ± 1.3	357.2 ± 18.6	2.03	176.0 ± 9.2	~16
πBG-V	688.5 ± 17.0	16.6 ± 1.2	440.5 ± 21.3	2.04	215.9 ± 10.4	~21
SBG-V	944.5 ± 46.6	20.6 ± 1.0	512.3 ± 24.5	2.07	247.5 ± 11.8	~27

Table S5. The thickness and mechanical properties of GO, rGO, G-PCO, πBG, and SBG sheets and the thickness and mechanical properties of GO-PCO sheets before and after UV irradiation.

Sample	Thickness (μm)	Young's modulus (GPa)	Tensile strength (MPa)	Toughness (MJ/m^3)	Strain to failure (%)
GO	7.6 ± 0.4	17.1 ± 1.1	151.3 ± 3.2	1.6 ± 0.1	2.3 ± 0.1
rGO	3.4 ± 0.2	8.0 ± 0.9	209.7 ± 8.0	2.6 ± 0.1	3.9 ± 0.2
GO-PCO before UV irradiation	8.2 ± 0.3	7.8 ± 1.2	157.2 ± 6.1	1.8 ± 0.1	2.4 ± 0.2
GO-PCO after UV irradiation	8.0 ± 0.4	7.6 ± 0.5	258.7 ± 2.8	5.5 ± 0.1	4.8 ± 0.1
G-PCO	3.8 ± 0.1	5.3 ± 0.6	348.5 ± 12.0	8.5 ± 1.3	6.8 ± 0.4
πBG-I	3.3 ± 0.3	6.9 ± 1.2	372.7 ± 16.4	9.4 ± 0.2	7.4 ± 0.4
πBG-II	2.7 ± 0.2	5.8 ± 0.6	502.4 ± 22.0	19.1 ± 1.9	10.3 ± 0.7
πBG-III	3.4 ± 0.2	10.6 ± 1.7	593.9 ± 24.5	16.5 ± 0.7	8.4 ± 0.5
πBG-IV	4.1 ± 0.2	9.1 ± 1.1	664.8 ± 27.0	14.6 ± 0.8	6.0 ± 0.3
πBG-V	3.7 ± 0.2	11.1 ± 1.2	688.5 ± 17.0	16.6 ± 1.2	5.5 ± 0.5
SBG-I	3.2 ± 0.1	7.0 ± 0.4	508.2 ± 24.3	14.9 ± 0.9	8.7 ± 0.5
SBG-II	3.2 ± 0.1	5.7 ± 0.5	702.7 ± 16.1	29.8 ± 2.1	11.5 ± 0.6
SBG-III	3.8 ± 0.2	13.3 ± 1.6	847.6 ± 23.0	25.4 ± 2.0	9.1 ± 0.4
SBG-IV	3.7 ± 0.2	18.5 ± 1.6	916.0 ± 25.0	22.1 ± 0.4	6.2 ± 0.4
SBG-V	3.3 ± 0.2	15.6 ± 1.0	944.5 ± 46.6	20.6 ± 1.0	5.9 ± 0.4

Table S6. The mechanical properties of SBG-V sheets, and other materials having high strengths in all sheet plane directions, including graphene sheet composites, carbon nanotube sheet composites, and carbon fiber composites.

Number	Materials	Tensile strength (MPa)	Toughness (MJ/m^3)	Reference
1	**Wet-spun rGO sheet**	172.2	0.8	(13)
2	**Collapsed graphene sheet**	22.5	1.7	(10)
3	**Debris-free graphene sheet**	60.0	4.8	(11)
4	**g-rGO**	614.0	14.9	(12)
5	**rGO-SL**	300.0	2.8	(34)
6	**rGO-PVA**	188.9	2.5	(29)
7	**rGO-PAA**	309.6	8.9	(36)
8	**rGO-PDA**	204.9	4.0	(24)
9	**rGO-PCDO**	129.6	3.9	(14)
10	**rGO-CS**	526.7	17.7	(27)
11	**rGO-PAPB**	382.0	7.5	(32)
12	**rGO-CNC**	655.0	1.8	(31)
13	**rGO-MoS_2-TPU**	235.0	6.9	(26)
14	**rGO-DWNT-PCDO**	374.1	9.2	(25)
15	**rGO-MMT-PVA**	356.0	7.5	(35)
16	**rGO-WS_2-PCDO**	413.6	17.7	(28)
17	**ai-rGO-CNC**	765.0	15.6	(30)
18	**T300-3K-PW/F655 BMI**	665.0	3.6	(38)
19	**AS4C-3K-PW/M65 BMI**	841.0	6.3	(38)
20	**AS4-3K-PW/8552 Epoxy**	793.0	4.8	(38)
21	**AS4-3K-5HS/8552 Epoxy**	800.0	4.8	(38)

22	**IM7-6K-PW/8552 Epoxy**	945.0	5.6	(38)
23	**IM7-6K-8HS/8552 Epoxy**	959.0	5.7	(38)
24	**T300-3K-8HS/F593 Epoxy**	563.0	2.8	(38)
25	**T300-3K-PW/F593 Epoxy**	637.0	3.6	(38)
26	**AS4C-6K-Twill/M21 Epoxy**	885.0	5.8	(38)
27	**T700-12K-Twill/M47 Epoxy**	900.0	6.6	(38)
28	**AS4-3K-Twill/M47 Epoxy**	930.0	6.3	(38)
29	**CHS-6K-Twill/M81 Epoxy**	870.0	5.6	(38)
30	**AS4C-3K-5HS/M92 Epoxy**	782.0	6.1	(38)
31	**AS4C-3K-PW/M92 Epoxy**	687.0	4.7	(38)
32	**SWNT-PEI-PAA**	175.0	0.9	(6)
33	**SWNT-PS**	51.0	0.4	(41)
34	**SWNT-Epoxy**	550.0	11.0	(43)
35	**MWNT-PEI-PAA**	165.0	4.6	(42)
36	**FDWCNT-Epoxy**	450.0	9.6	(40)
37	**MWNT-BMI**	620.0	7.8	(39)
38	**SBG-V**	944.5	20.6	This work

Table S7. The *D/G* Raman intensity ratios for GO, rGO, GO-PCO, G-PCO, πBG-V, and SBG-V sheets using 633 nm excitation.

Sample	*D/G*
GO	1.15
rGO	1.61
GO-PCO	1.37
G-PCO	1.69
πBG-V	1.62
SBG-V	1.69

Table S8. The O_{1s}/C_{1s} atomic ratios for GO, rGO, GO-PCO, G-PCO, πBG-V, and SBG-V sheets.

Sample	O_{1s}/C_{1s} (atomic ratios)
GO	0.45
rGO	0.19
GO-PCO	0.41
G-PCO	0.16
πBG-V	0.17
SBG-V	0.16

References

S1. Okawa Y, Takajo D, Tsukamoto S, Hasegawa T, Aono M (2008) Atomic force microscopy and theoretical investigation of the lifted-up conformation of polydiacetylene on a graphite substrate. *Soft Matter* 4:1041-1047.